Journal of Metals, Materials and Minerals, 35(4), e2405, 2025

Facile bio-synthesis of cerium oxide nanoparticles, characterization and their photocatalytic potential in the degradation of real tannery wastewater

Ganeshkumar GOVINDASAMY[1], and Arjunan Babu PONNUSAMI[1,*]

[1] *School of Chemical Engineering, Vellore Institute of Technology, Vellore – 632014, Tamil Nadu, India*

***Corresponding author e-mail**: ababuponnusami@vit.ac.in

Received date:
15 May 2025
Revised date:
17 June 2025
Accepted date:
15 July 2025

Keywords:
Cerium oxide;
Bio-synthesis;
Photo catalysts;
Nanoceria particles;
Peepal leaves

Abstract

The sustainable metal oxide photocatalysts using plant extract presents a viable alternative to conventional chemical synthesis techniques. In this study, spherical shaped cerium oxide nanoparticles were synthesized using ammonium ceric nitrate and *Peepal leaves* extract and used as a photo-catalyst to remove hexavalent chromium and chemical oxygen demand from actual tannery wastewater. The characterization of cerium oxide nanoparticles was carried out using UV-Visible spectroscopy, X-ray diffraction, Fourier-transform infrared spectroscopy, Brunauer-Emmett-Teller surface area analysis, Field Emission-Scanning Electron Microscopy with energy-dispersive X-ray spectroscopy, Raman analysis, High Resolution-Transmission Electron Microscopy and Zeta potential analysis. The band gap energy of 3.25 eV was observed through TAUC plot and the BET surface area, pore volume and pore diameter were measured as 33.545 $m^2 \cdot g^{-1}$, 0.094 $cm^3 \cdot g^{-1}$, and 1.433 nm respectively, indicates the characteristics of mesoporous photocatalyst. 77.2% of chemical oxygen demand and 84.5% of chromium (VI) removal was observed at an optimal condition of pH 7, H_2O_2 concentration 0.0195 mL and cerium oxide dosage of 0.04 g/250 mL. The experimental results were well fitted with the pseudo-first order kinetics with the rate constant values of 0.0597 min^{-1} with the R^2 value of 0.9906. Also, the repeatability studies demonstrate that the cerium oxide nanoparticles are found to be unaffected. These studies confirmed that the nanoparticles produced through bio-synthesis method are potential photocatalyst for treating real tannery wastewater.

1. Introduction

Industrialization has experienced a remarkable surge, leading to the expansion of the economy and improvement in quality of life [1]. As industrialization rapidly advances, a growing amount of new organic pollutants such as heavy metals, drugs, and dyes has been generated and released into aquatic ecosystems, significantly degrading the natural water environment [2]. Surface water bodies play a crucial role in meeting water demand for industrialization, supporting economic development, and facilitating ecological restoration [3]. The global water demand is experiencing rapid geometric growth, surpassing the availability of freshwater by 20% to 30% prior to the year 2050 [4]. As a result, the issue of global shortage of water and water constrained is becoming increasingly urgent, causing worry among political and scientific organizations. Henceforth, the availability of water for the global population witnessed a decline from 12,900 m^3 in 1970 to below 7000 m^3 in 2000. Furthermore, it is anticipated that this will further decrease to 5100 m^3 per capita per year by 2025 [5]. By 2030, the aspiration of Sustainable Development Goal 6 (SDG) was to achieve and ensure access to pure, ample, affordable water and along with standard conditions for everyone [6]. Clean and plenteous water are fundamental concerns that intersect with all sustainable achievements, related to all living things on our planet [7]. Water quality and adequate quantities are essential rights for all humans and important subjects for any kind of progress [8]. To alleviate the serious water shortage, the utilization of wastewater reuse, reclamation, and recycling shows exciting potential. Nevertheless, the worldwide practices of reclaiming and reusing wastewater are severely insufficient. Over 80% of wastewater worldwide is released into the surrounding environment without proper or sufficient treatment [9]. The plant's treatment efficiency is commendable when it comes to removing conventional pollutants. Heavy metals, including Cr, Pb, and Cu, can function as carcinogens due to the presence of the azo group. They also disrupt physiological processes in the human body. Additionally, aquatic life is adversely affected by rising BOD levels, which lead to reduced oxygen content and impede the photosynthetic activity of aquatic plants [10]. However, it has shown incompatibility in its ability to remediate heavy metals, such as chromium [11]. Chromium plays a vital role in numerous industries, especially in the leather tanning sector. It serves as the primary chemical component required for the tanning process [12].

The tannery industry contributes to environmental pollution through the release of both organic and inorganic substances [13,14]. The usage of chemical reagents is extremely high [15]. There are numerous chemicals that are commonly used as inputs, including sodium chloride, lime, basic chromium, sulphuric acid, fats, detergents, biocides, and several others [16]. Many of these chemicals do not get absorbed during the tanning process and are released into the effluents [17]. More than 90% of the leather industries globally utilize chromium

as tanning medium. Raw salt of chromium can take on various forms such as hydrogen chromate ($HCrO_4^-$), dichromate ion ($Cr_2O_7^{2-}$), chromate ion (CrO_4^{2-}) and which are the responsible for the pH level of the reaction mixture, as pH: (2 to 6), (6 to 8), and (>8) respectively [18]. Cr (VI) is known to be the most hazardous, soluble, and easily transportable species [19]. Leather based wastewater is the main cause of Cr(VI) contamination in both soil and water, thereby impacting two crucial components of the environment [20]. The allowable discharge limit of Cr(VI) into surface water bodies cannot exceed 0.05 mg·L^{-1} [21]. The reactivity of Cr (VI) is highly delicate and harmful to the environment. Typically, it has the potential to induce negative long-term and immediate impacts on other organisms [22].

There are several advanced methods for treating wastewater, including Advanced Oxidation Processes (AOP), electrodialysis, ion exchange, reverse osmosis, chemical precipitation, disinfection, adsorption, photocatalysis, electrocoagulation, and membrane separation [23,24]. The advanced oxidation processes have been receiving more recognition for its effectiveness in breaking down organic wastes by generating highly reactive hydroxyl radicals (•OH) and hyperoxide radicals (•O_2^-) [25]. Photocatalysis exhibits immense potential as an innovative technology for effectively eliminating heavy metals. A key area of contemporary research in photooxidation methods involves the development of advanced photocatalysts capable of efficiently producing reactive oxygen species [26]. Additionally, photocatalysis proves to be easy to plan, versatile, economically viable, environmentally friendly, controllable, technically feasible, and effective as a treatment method [27,28]. Here, the organic hazardous matter gets complete mineralization depends on the factors including absorption spectra, irradiation source and its wavelength [29]. Photocatalysis provides the conversion between light energy into reactive chemical energy [30]. Semi-conductors based heterogeneous photo-catalysis has been recognized as a suitable, environmentally friendly, and globally relevant technology [31]. Photocatalysts are unveiling photons by a specified source, because of their bandgap energy. As a result, the electrons (e^-) create holes when they transfer from valence band to conduction band [32]. Consequently, the interaction between h^+ and OH^-/H_2O, leads to the formation of hydroxy radical (•OH), while the reaction between e^- and oxygen results in the generation of superoxide radical (•O_2^-) [33].

Various metal oxides and sulfides have been studied as photo-catalysts, such as cerium dioxide [34], molybdenum disulfide [35], titanium dioxide [36], iron sulfide [37], bismuth oxobromide [38], tungsten trioxide [39], nickel oxide [40], copper indium sulfide [41], and zinc oxide [42], and polymer based C_3N_4 and C_3N_5 photocatalysts [43]. Rare-earth based materials are attracting researchers because they have the 4f orbit partial fulfillment. Due to its exceptional qualities, it is extensively utilized in numerous industrial applications, highlighting its superiority in these aspects. Nanoceria (CeO_2) has been primarily selected for various purposes including catalysts, semi-conductors and sensors, polishing materials, energy-related utilizations, optical tools, diesel fuel additives and among others [44]. In this study, the synthesis of cerium dioxide nano photocatalyst material was effectively accomplished using a one-pot bio-synthesized with precipitation technique. Nanoparticles generated via this bio-synthesis approach exhibit enhanced safety, stability, and biocompatibility compared to those created through traditional physical or chemical methods. The application of this method resulted in a remarkable degradation rate of Chemical Oxygen Demand (COD) in tannery wastewater, reaching 88.9% within a duration of 150 min [45]. Hence, the objective of this investigation was to reduce chromium and COD present in tannery industrial effluent by biosynthesized CeO_2 nano-particles. The parameters involved in optimizing the process are catalyst dosage, H_2O_2 concentrations, pH, Contact time, and the initial concentration.

2. Materials and methods

2.1 Materials

Ammonium ceric nitrate ($H_8N_8CeO_{18}$), Sulphuric acid (H_2SO_4), Sodium hydroxide (NaOH), Potassium dichromate ($K_2Cr_2O_7$) are purchased from Sigma-Aldrich (99.9%). Acetone (CH_3COCH_3), Ethyl alcohol and Methanol (CH_3OH) are received from Merck (99.9%) and used without further purification. All the experiments were conducted using Millipore water. Real tannery wastewater samples were collected from the industrial sector in Ranipet Sipcot, which is located near the Vellore District in Tamil Nadu, India. The polyethylene sample containers washed multiple times with deionized water were used for collecting the wastewater samples twice a month on a basis. The samples were preserved in the refrigerator immediately at a temperature of 4°C and the characterization was carried out as per standard methods [46]. The specifications of tannery wastewater are shown in Table 1.

2.2 Preparation of cerium oxide nano photocatalyst

The cerium oxide nano particles were produced through bio-synthesis process and is illustrated in Figure 1. Ammonium ceric nitrate (0.1 M) was used as precursor for the synthesis of cerium oxide nanoparticles through hydroxide mediated method. *Peepal leaves (Ficus Religiosa)* extract was used as a reducing agent to prepare

Table 1 Actual tannery wastewater specifications

Parameters	Range of values
pH	2.9 – 3.4
Cr(VI) [mg·L^{-1}]	125 – 145
Biochemical oxygen demand [mg·L^{-1}]	1450 – 1650
Dissolved oxygen [mg·L^{-1}]	2.0 – 2.3
Turbidity [NTU]	150 – 175
Total dissolved solids [mg·L^{-1}]	2250 – 2350
Total solids [mg·L^{-1}]	5000 – 5150
Chemical oxygen demand [mg·L^{-1}]	3280 – 3450

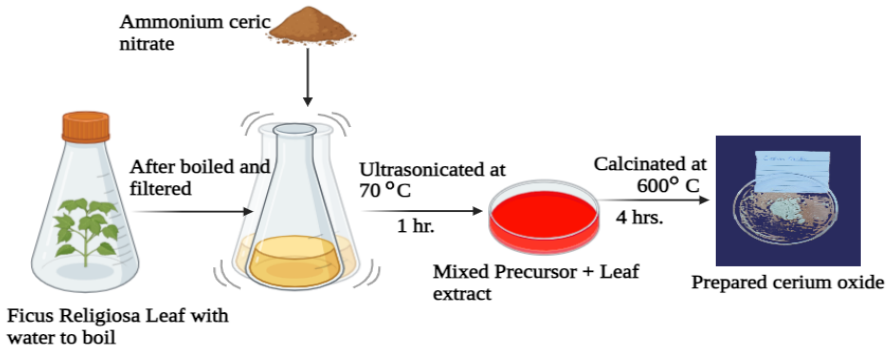

Figure 1. Synthesis of cerium oxide nanoparticles through bio-synthesis.

Figure 2. Bio-synthesized Cerium Oxide nanoparticles.

cerium oxide nano particles. The pH of the mixture is 12 using NaOH. Then, mixture gets dissolved under magnetic stirring for 2 h at room temperature. Then the mixture solution was ultrasonicated for 1 h at 70°C to 80°C. After ultrasonication, the solution was allowed to centrifugation for 10 min at 5000 rpm to precipitate cerium particles. The precipitated semi solid particles were washed with ethanol and distilled water until the pH was neutralized. Then it was allowed to oven at 80°C for around 7 h to 8 h and reduced size using Mortar and Pestle. The cerium particles were calcined at 600°C for 4 h to produce cerium oxide nano particles as shown in Figure 2 [47].

The characteristics of the nanomaterial were determined using UV-vis spectrometer (model: JASCO V-670), which operates within a wavelength range of from 200 nm to 2600 nm. An XRD analysis (model: Bruker D8 Quest, Germany), as employed to analyze the composition and purity of the mixtures phase structure within the range of 20° to 70°. The identification of functional groups present on the surface of the nanomaterials was done by using FTIR, (model: Shimadzu, Japan) within the range of 500 cm^{-1} to 3900 cm^{-1}. Average particle size and potential particle distribution of the CeO_2 nanoparticles were confirmed through zeta potential analysis using the SZ-100 model from Horiba Scientific for Dynamic Light Scattering (DLS) analysis. The surface topography was analyzed using Field Emission Scanning Electron Microscope (FE-SEM) (Model: ZEISS EVO 18) and the components present as well as composition at different magnifications were analyzed using energy dispersive analysis. BET surface area and pore size distribution were determined using Quanta chrome analyzer (model: AutosorbiQ - USA) analyzer with the valid range of 33.545 $m^2 \cdot g^{-1}$ [48].

2.3 Mechanisms involved in photocatalytic approach using cerium oxide

Photodegradation involves semi-conducting materials acting as photo-catalytic materials, capturing energy as photons that surpass their bandgap values. The process of absorption results in the separation of charges, an-electron moves from Valence State (VS) to Conduction State (CS) of catalytic material, consequently, creates hole in the valence state. Produced electron-pairs and reactions help to surpass the energy band gap level. Due to the intense oxidation, highly reactive free radicals were formed. Cerium dioxide (CeO_2) has emerged as a highly effective photocatalyst for oxidative degradation, offering a potential solution to the challenges posed by energy scarcity and environmental contamination. During the photocatalytic degradation of organic molecules in waste-water, the photoexcitation of CeO_2 in aqueous solution results in the generation of various radicals and charged species as described as (Equations (1-6)) [49,50]. Finally, the wastewater gets degraded into water and carbon di-oxide molecules.

$$CeO_2 + h\upsilon \rightarrow CeO_2 + h^+ + e^- \quad (1)$$

$$e^- + O_2 \rightarrow {}^{\bullet}O_2^- \quad (2)$$

$$H_2O \rightarrow {}^{\bullet}OH + H^+ \quad (3)$$

$$h^+ + OH^- \rightarrow {}^{\bullet}OH \quad (4)$$

$$e^+ + H_2O_2 \rightarrow {}^{\bullet}OH + OH^- \quad (5)$$

$$H_2O_2 + CeO_2(e_{CB}^-) \rightarrow CeO_2 + {}^{\bullet}OH + OH^- \quad (6)$$

2.4 Experimental approach

The photocatalytic degradation of tannery effluent was allowed in batch-processes [51]. The capabilities of cerium oxide nanoparticles examined the reducing chromium levels and chemical oxygen demand. The study focused on several parameters, including catalyst dosage (ranging from 0.01 $g \cdot L^{-1}$ to 0.05 $g \cdot L^{-1}$), initial COD concentration (between 100 ppm and 500 ppm), pH levels (from 3 to 9), and H_2O_2 dosage (spanning 0.0075 mL to 0.0235 mL). The studies on photo-catalytic ability performed in a 500 mL reactor vessel, using Ultraviolet (UV) irradiation lamps produced by Philips, Holland. 18 W of three lamps, wavelength (λmax) = 250 nm to 255 nm were used [52].

Temperature kept the ranges of 22°C to 26°C with the aid of water circulation. The gap maintains in the range of sample to ultraviolet light being 15 cm. Light intensity of ultraviolet light measured by Lux light meter (LX-1102, manufactured by Lutron Electronic.). The measurement of ultraviolet light intensity reached in the ranges of 0.295 $W \cdot m^{-2}$ to 0.297 $W \cdot m^{-2}$ [53]. Aliquots were collected and allowed centrifuge process. Supernatant liquid isolated and allowed to COD measurements by open reflux method. Chromium(VI) was assessed by withdrawing a particular volume of the sample and allowed us to react with the solution of 1,5-diphenyl carbazide reagent [54]. The chromium concentration in 1,5-Diphenyl carbazide-Chromium(VI) mixture was quantified using atomic absorption spectroscopy (Model: Perkin-Elmer ANALYST 400. The percentage of chemical oxygen demand & chromium (VI) reduction was calculated using Equation (7-8).

$$\text{Percentage of COD reduction} = \frac{\text{Initial COD in } (mg \cdot L^{-1}) - \text{Final COD in } (mg \cdot L^{-1})}{\text{Initial COD in } (mg \cdot L^{-1})} \times 100 \quad (7)$$

$$\text{Cr(VI) reduction (\%)} = \frac{\text{Initial Cr(VI) value } (mg \cdot L^{-1}) - \text{Final Cr(VI) value } (mg \cdot L^{-1})}{\text{Initial Cr(VI) value } (mg \cdot L^{-1})} \times 100 \quad (8)$$

2.5 Kinetic study

2.5.1 Pseudo-first order kinetic model

Kinetic analysis plays a vital role in photocatalysis, offering important insights into how different factors such as pH, cerium oxide input, and volume of H_2O_2 effect on process. The "Pseudo first order rate equation" and the "Lagrangian fir equation" are both utilized in data analysis. The reactions do not genuinely adhere to first-order kinetic model, and display traits of first-order behavior because one or more reactants are present in much higher concentrations than the others are known as pseudo-first-order kinetics. The review of existing literature revealed that the photocatalytic degradation of wastewater follows pseudo-first-order kinetics [55]. When one of the reactant molecules is present in a substantial excess, the apparent order of the reaction may not accurately reflect the actual order of the reaction. The sequence that is observed, that does not align with the actual sequence, is referred to as the Pseudo first-order. References suggest that the existing system operates under a pseudo first and second-order mechanism, as illustrated in the equations below. The degradation rate of actual wastewater (ww) for the current study is presented in Equation (9).

$$\text{Rate of degradation} = -\frac{dC_{WW}}{dt} = \sum_i^n C_{WW} C_{Oxi}\, k_{Oxi} + K_{HO} C_{OH} C_{WW} \quad (9)$$

In this context, Oxi refers to species other than •OH. Given that the concentrations of hydroxyl radicals are greater than those of the other components, the hydroxyl radicals solely influence the rate equation. Therefore, the equation presented above can be expressed as:

$$\text{Rate of WW degradation} = -\frac{dC_{WW}}{dt} = K_{HO} C_{OH} C_{WW} \quad (10)$$

The concentration of the reactive element reaches equilibrium quickly, resulting in a stable presence of •OH based on the reacting conditions. Consequently, rate of sample degradation follows pseudo-first order kinetic model, characterized by a concentration of •HO radicals [56].

$$\text{Rate of WW degradation} = -\frac{dC_{WW}}{dt} = K_1 C_{WW} \quad (11)$$

The rate constant of pseudo-first order is represented as $K_1 = K_{OH} C_{OH}$. (Equation (11)) is allowed to integrate, and we get.

$$\ln C_{WW} = \ln C_{WW_0} - K_1 t \quad (12)$$

Upon rearranging, the above equation can be expressed as the pseudo first-order equation.

$$\text{In} \left(\frac{C_{WW_t}}{C_{WW_0}}\right) = -K_1 t$$

$$-\text{In} \left(\frac{C_{S0}}{C_{Si}}\right) = -K_1 t \quad (13)$$

Where C_{si} and C_{so} are the initial and final chemical oxygen demand of the wastewater sample.

2.5.2 Pseudo-second order kinetic model

The Pseudo-second order model is generally represented as a curvilinear function, which can be articulated in a differential form as follows:

$$\frac{dq}{dt} = K_2 (q_e - q)^2$$

An integration conducted under the specified constraints, where at time t = 0, q = 0, at time t = t, $q_e - q = q_t$, can yield various distinct yet interconnected linear transformations of the pseudo-second order models.

$$q = \frac{t}{\frac{1}{k_2 q_e^2} + \frac{t}{q_e}}$$

$$\frac{q}{t} = \frac{k_2 q_e^2 q_e}{q_e + t k_2 q_e^2}$$

$$q = \frac{k_2 q_e^2 t}{1 + t k_2 q_e}$$

$$\text{or} \quad \frac{t}{q} = \frac{t}{q_e} + \frac{1}{K_2 q_e^2}$$

$$\frac{t}{q} = \frac{t}{q_e} + \left[\frac{1}{K_2 q_e^2}\right]\frac{1}{t}$$

$$q = q_e - \left[\frac{1}{K_2 q_e}\right]\frac{q}{t}$$

$$\frac{q}{t} = k_2 q_e^2 - k_2 q_e q$$

$$\frac{1}{q_e - q} = \frac{1}{q_e} + k_2 t$$

Modify the above equation,

$$\frac{1}{[C_{so}]} = \frac{1}{C_{si}} + k_2 t \quad (14)$$

The initial and final concentration of COD of wastewater sample represented by C_{si} and C_{so} respectively. The distribution of the error function necessary for evaluating the robustness of the pseudo-second order kinetic model is contingent upon the specific linearization technique employed for the non-linear form. Yu *et al.* reported that the removal of Pb^{2+} from synthetic wastewater using carboxylate nanocellulose crystals followed a pseudo-second order kinetic model [57]. Whereas the removal of Cr(VI) from wastewater using calcium hydroxyapatite and micro fibrillated cellulose was effectively described by the pseudo-second order kinetic model [58]. Hao *et al.* also reported that the elimination of As(V) and P(V) ions from aqueous solutions using polyethyleneimine and ferric ion-coated spent coffee powder followed a pseudo second-order kinetic model [59].

2.5.3 Diffusional and Singh model kinetic system

The study determinates the removal of chemical oxygen demand through the photocatalytic reaction [60]. The diffusional model can be written as the Equation below.

$$\frac{-dC_s}{dt} = K_3 C_{si}^{0.5} \quad (15)$$

After integration of the above equation within the known limits, we get.

$$\sqrt{C_{si}} - \sqrt{C_{so}} = K_3 t \quad (16)$$

Here K_3 is the diffusional model kinetic rate constant.
The Singh kinetic rate model can be written as:

$$\frac{-dC_s}{dt} = \frac{K_4 C_{si}}{1+t} \quad (17)$$

After integrating the above equation within the known limits, we get the final Singh model Equation.

$$\mathrm{Ln}\left[\frac{C_{si}}{C_{so}}\right] = -K_4 \mathrm{In}(1+t) \quad (18)$$

Here K_4 is the Singh model rate constant.

3. Results and discussions

3.1 Ultraviolet visible light spectroscopy analysis

The UV-Visible absorption spectra of cerium oxide particles and *Peepal leaves* extract were recorded within the wavelength range of 200 nm to 500 nm. The particles underwent ultrasound treatment for a duration of 30 min prior to the analysis [21]. The UV-visible spectra for nanoceria particles and PL extract are presented in Figure 3(a-b), respectively. Observations indicated that the band-gap absorption of CeO_2 nanoparticles, attributed to electron transitions between the conduction band (CB) and valence band (VB), exhibited the prominent peak at 335 nm, closely aligning with the absorption characteristics of bulk nanoceria particles. Naturally, plant extracts contain cellulose, flavonoids, starch, alginate, hyaluronic acid, and chitosan are used as stabilizers for various metal nanoparticles prepared by bio-synthesis methods [61]. The findings demonstrated that, PL extracts functioned as a capping cum stabilizing agent for CeO_2 nanoparticles [62]. The cerium oxide band gap energy determined using the TAUC plot illustrated in Figure 3(c). The photon energy of the nanoparticles is calculated using the following (Equation (19)).

$$E_g = \frac{hc}{\lambda} \quad (19)$$

In this context, h - represents Planck's constant, c - denotes the speed of light, and λ signifies the wavelength that is being adsorbed. Figure 3(c) illustrates that the maximum value was achieved at a photon energy level of 5.39 eV [63]. The bandgap of cerium oxide is determined by extending the linear-portion of the graph in the x-axis, resulting in a measurement of 3.25 eV. Comparable values have been documented in literature [64,65].

3.2 Stability of cerium oxide by zeta potential analysis

The outcomes from dynamic light scattering indicated that the average zeta potential value of cerium oxide nanoparticles was measured at −25.5 mV, see the illustration as Figure 4. The hydrodynamic zeta potential (ζ) was measured in aqueous suspensions of the samples at a concentration of 1 mg dissolved in 1 mL of ultra-pure water [66]. Prior analysis, the sample allowed sonication for a duration of 30 min to 45 min. The size distribution plots based on % Number intensity and the ζ-potential distribution by Total counts are shown as average distribution values derived from three consecutive measurements, each taken at 10 s intervals, for both 10 run and 20 run. The findings indicated that the zeta potential values varied from –23.93 mV to –28.65 mV as shown in Table 2. The mean value of cerium oxide as – 25.49 mV, with a standard deviation of 2.05 mV, indicating the presence of (–) ve charge in the dispersed mixture. The production of nanoparticles from Peepal leaf extract containing more organic functional groups are interacts on the ammonium ceric nitrate precursor, which may explain the differences observed in zeta potential values and the stability of the material in various sample runs.

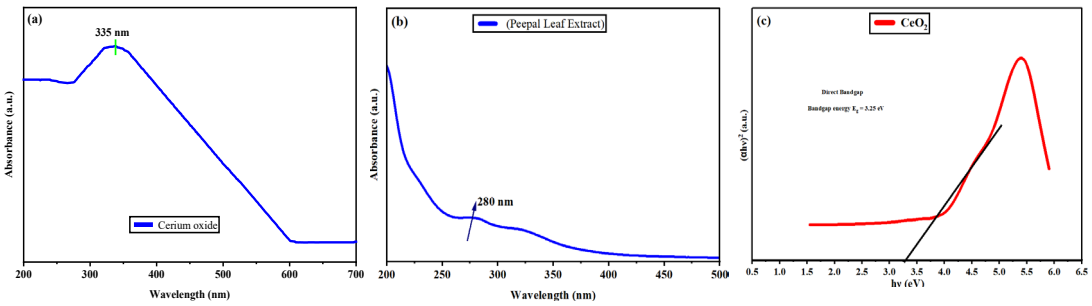

Figure 3. UV-visible analysis of (a) cerium oxide particles, (b) PLE, and (c) bandgap value of cerium oxide by TAUC's plot.

Table 2. Average particle size of cerium oxide by zeta potential analysis.

Runs	Zeta-potential values [mV]	Mobility values [(μ·s^{-1})/(V·cm^{-1})]	Mean values [mV]	Average zeta potential [mV]
Sample run 1	-25.49	-1.99	-23.18	-25.5
Sample run 2	-28.65	-2.20	-25.13	
Sample run 3	-24.35	-1.87	-22.27	
Sample run 4	-25.05	-1.90	-23.20	
Sample run 5	-23.93	-1.62	-22.59	

Table 3. Particle size calculation from Scherrer Equation.

Peak position [2θ]	Miller's index position	FWHM [°]	β in [radians]	Crystal size [nm]
28.74	(111)	0.29	0.0050	30.00
30.56	(200)	0.30	0.0052	29.12
42.89	(220)	0.41	0.0071	22.08
51.88	(222)	0.45	0.0078	20.83
62.33	(311)	0.49	0.0085	20.10
72.79	(400)	0.52	0.0090	20.05

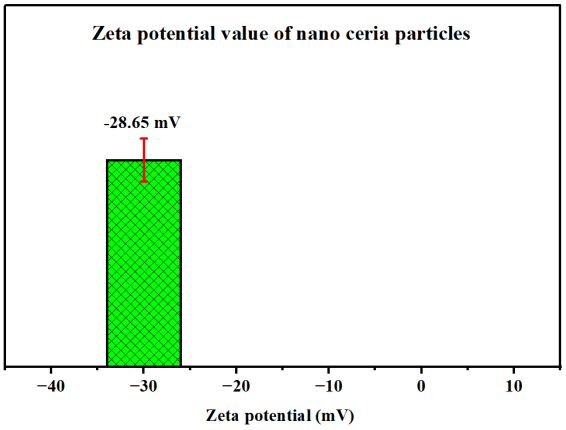

Figure 4. Zeta potential value of cerium oxide.

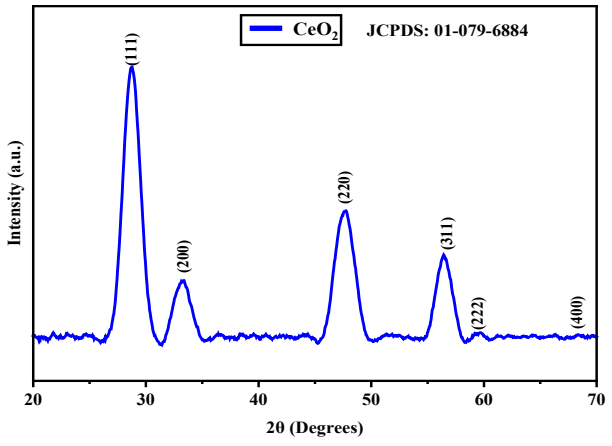

Figure 5. Cerium oxide's X-ray diffractogram.

3.3 X-Ray powder diffraction analysis

X-ray diffraction (XRD) is a widely utilized and dependable technique for characterizing nanoparticles, particularly in assessing their dimensions, crystalline structures, and phase angles. Different crystalline structures produce distinct diffraction patterns of X-rays, which are referred to as diffraction patterns. The XRD pattern, also known as the diffractogram, is obtained by measuring over a spectrum of angles (2θ). Every peak observed in the XRD pattern is associated with a particular crystallographic plane within the crystal lattice of the nanoparticle. The differences in structure are acknowledged to be some significant parameters such as dislocation of line densities and grain size. The Scherrer formula can be utilized to ascertain the grain sizes (D) as shown in (Equation (20)). In this context, Constant K represents the shape factor of 0.954, while λ, equal to 1.541 Å, denotes the wavelength of the X-rays [67]. Additionally, β refers to the Full Width at Half Maximum (FWHM) measured in radians, and the peak position is indicated in θ (degrees), the values are summarized in Table 3. The measured 2θ values correspond to the hkl indices (111), (200), (220), (311), (222), and (400) in the specified sequence (Figure 5), indicating that the spherical crystallite's structure is face-centered cubic symmetry. The findings of this XRD analysis are consistent with the previous research conducted by other researchers [68]. The average crystal size evaluated from the Scherrer formula is 23.70 nm. Significantly, the lack of any peaks associated with impurities further validates the effective synthesis of high-purity cerium oxide nanoparticles [69].

$$D = \frac{K\lambda}{\beta \cos\theta} \tag{20}$$

3.4 Raman spectroscopy analysis

Bulk CeO_2, characterized by its spherical structure, displays a prominent Raman peak at 452 cm^{-1}. This peak corresponds to the triply degenerate F2g mode, which represents the symmetric stretching vibrations of oxygen ions surrounding Ce^{4+} ions within the octahedral CeO_8 configuration, classified under the two symmetric elements. It is extremely susceptible to disorders associated with oxygen. The Raman spectrum of CeO_2 nanoparticles (Figure 6) displays a prominent, broadened Raman absorption peak at 452 cm^{-1}, along with weaker absorption peaks observed at 612 cm^{-1} and 1054 cm^{-1}. The presence

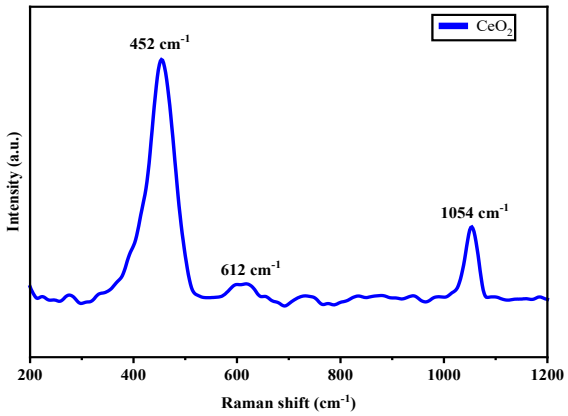

Figure 6. Raman spectra of nanoceria particles.

of the Raman peak at 452 cm^{-1} validates the spherical structure of the synthesized CeO_2 nanoparticles. The width of the peak suggests that the size of the particles is small. The peak exhibits asymmetric broadening and a minor shift towards the lower energy side, which can be attributed to the existence of oxygen vacancies [70]. Oxygen vacancies are classified as point defects, which primarily lead to the widening of the peaks observed in the Raman spectrum. The prominent peaks observed at 612 cm^{-1} and 1054 cm^{-1} can be attributed to the existence of oxygen vacancies [71]. In the cubic fluorite arrangement of CeO_2, the oxygen ions are not densely packed. At higher temperatures, CeO_2 has the potential to release oxygen through a specific reaction such as (Equation (21)) and create countless oxygen vacancies while maintaining the fundamental cubic symmetrical spherical structure. The surplus electrons produced during the process are reallocated to the cation void levels, therefore resulting in a change of their oxidation state from Ce^{4+} to Ce^{3+}. The effectiveness of ceria as a redox catalyst and as an oxygen storage medium is significantly influenced by the presence of oxygen vacancies. Arumugam *et al.* reported that the cerium oxide nanoparticles derived from gloriosa superba leaf extract and the Raman peak of 457 cm^{-1} as recorded [72].

$$2CeO_2 \rightarrow Ce_2O_3 + \frac{1}{2}O_2 \quad (21)$$

3.5 Fourier transform infrared spectrum analysis

By the principle of infrared beam applications, Fourier-transform infrared spectroscopy was utilized to analyze the specific functional groups that are responsible for the development of materials. Infrared radiation quantified by an individual bond in a molecule resulting in a spectrum of image displaying the wavenumber versus transmittance percentile [73]. The FTIR spectrum of the Peepal leaf extract and prepared nanoceria of after reaction and before reaction was illustrated in Figure 7(a-b) respectively, both the spectrum showing a range from 4000 cm^{-1} to 500 cm^{-1}, it revealed the existence of different functional groups and bonds in the nanoceria. In Figure 7(b), different peaks were detected at 3476 cm^{-1}, 1712 cm^{-1}, 1627 cm^{-1}, 1427 cm^{-1}, 1176 cm^{-1}, 1098 cm^{-1}, 992 cm^{-1} and 543 cm^{-1}, also the extensive absorption band of nano cerium seen spanning from 3667 cm^{-1} to 3007 cm^{-1} is associated with the stretching vibration of OH or potentially with the impact of water molecules absorbed on the sample surface [74]. The absorption peak observed at around 3476 cm^{-1} is associated with the O–H stretching of the metal hydroxide phase [75].

Another absorbance peaks observed at 1712 cm^{-1} and 1627 cm^{-1} correspond to the bending of H–O–H and the stretching vibrations of C–H, respectively [76]. Additionally, the peak associated with Ce–O stretching vibrations was observed at 992 cm^{-1}, 701 cm^{-1}, and 543 cm^{-1} [77]. The absorption peaks of CeO_2 nanoparticles from Figure 7(b), after degradation indicate the emergence of a new peak corresponding to the Ce–O bond at a wavelength of 526 cm^{-1}. Additionally, there is a notable shift in the peak associated with the O–Ce–O bond at 931 cm^{-1}, 675 cm^{-1}, and 538 cm^{-1}, which exhibits increased intensity, while the peak related to N–O stretching of nitrate, ranging from approximately 1000 cm^{-1} to 1300 cm^{-1}, shows a reduction in intensity. The findings of this research align with those reported by Arumugam *et al*., who similarly identified the maximum Ce–O stretching at 451 cm^{-1} [72].

3.6 Surface area and pore size analysis of cerium oxide

The adsorption characteristics of the adsorbent were significantly affected by the surface area, pore volume, and pore diameter. The properties for cerium oxide are surface area, pore volume and pore diameter as detailed in Table 4, were measured at 33.545 $m^2 \cdot g^{-1}$, 0.094 $cm^3 \cdot g^{-1}$, and 1.433 nm, respectively. The BET, surface area and porosimeter analyzer was utilized to assess the surface area and porosity of cerium oxide. The degassing process of cerium oxide was conducted at a temperature of 250°C for a duration of 3 h. The mixture of nitrogen (N_2) and helium (He) gases was utilized for the analysis of the area. N_2 adsorption isotherms were measured at –196°C [78]. The surface area was determined using the multi-point BET method, which is based on the adsorption of nitrogen gas on the surfaces of cerium oxide, within a relative pressure p/p_0 range from 0.05 to 0.33.

The isotherms were categorized based on the standards set by the International Union of Pure and Applied Chemistry (IUPAC). The total pore volumes, (Vp), were determined through single-point adsorption measurements conducted at a relative pressure of approximately 0.99. Pore Size Distribution (PSD) were assessed through the adsorption and desorption branches of the nitrogen isotherm by employing the Barrett-Joyner-Halenda (BJH) method [79]. The analysis conducted using the BJH model indicates an average pore size ranging from 14 nm to 25 nm, along with a cumulative pore volume of 0.094 $cm^3 \cdot g^{-1}$. For cerium oxide, the adsorption isotherm is classified as type IV, characterized by a lower adsorption value at low relative pressures (0.02 to 0.8), followed by a sharp increase in the adsorption rate at higher values (greater than 0.85). The isotherm curves for the synthesized pure CeO_2 display a typical type IV pattern, indicating the existence of mesopores. Comparable findings were reported by Parameswaran *et al.* in their study on the efficacy of cerium oxide and the isotherms are shown in Figure 8 [80]. Furthermore, the specific surface area does not play a crucial role in the catalytic activity of nanoparticles, however, acidic or neutral pH conditions facilitate improved performance. Despite having small specific surface areas and low concentrations of catalysts, nanoparticle facilitates removal rates approaching 100% in advanced oxidation processes [81]. Neus *et al.,* reported that the magnetite catalyst (Fe_3O_4), used for the azole pesticide degradation as 80% under the optimum conditions of pH = 5, H_2O_2 = 6.7 $mg \cdot L^{-1}$, at room temperature with the specific surface area of the particle was 7.5 $m^2 \cdot g^{-1}$ [82].

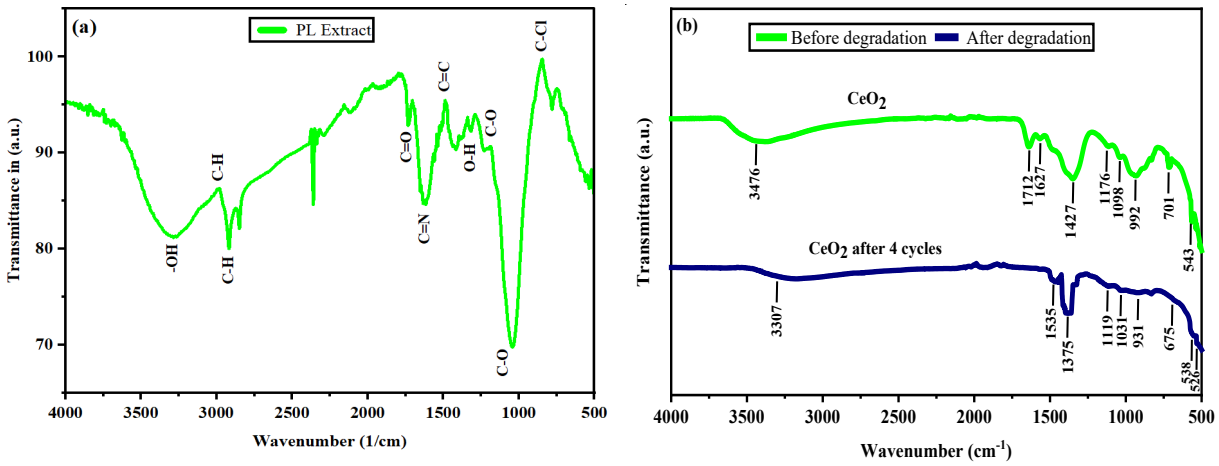

Figure 7. FTIR spectrum of nanoceria calcined at 650°C.

Table 4. BET analysis data of cerium oxide.

Notations	Nanoceria particles
Surface area [$m^2 \cdot g^{-1}$]	33.545
Pore diameter [nm]	1.433
Pore volume [$cm^3 \cdot g^{-1}$]	0.094

Table 5. EDAX details of cerium oxide nanoparticles.

Elements	Weight percentile [%]	Atomic percentile [%]
Ce	53.63	10.88
O	34.95	62.11

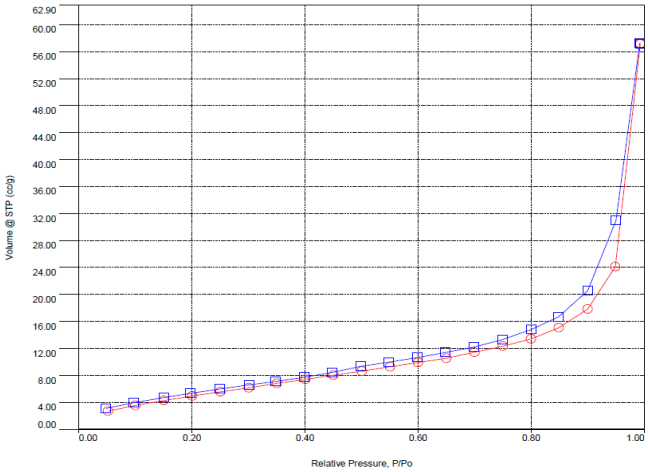

Figure 8. The isotherms of nanoceria particles.

3.7 Field emission scanning electron microscopy and high-resolution transmission electron microscopy

The FE-SEM image depicting the synthesized CeO_2 nanoparticles is presented in Figure 9(a) and indicates that the particles exhibit a spherical shape and are agglomerated. The particle size, as determined from the FE-SEM image, ranges from 13 nm to 30 nm. The EDAX spectrum for CeO_2 nanoparticles is illustrated in Figure 9(b). The EDAX spectrum confirms the existence of oxygen and cerium elements within the synthesized CeO_2 nanoparticles. The elemental makeup of CeO_2 nanoparticles is approximated to consist of cerium (Ce), oxygen (O), along with the remaining portion being carbon as shown in Table 5. CeO_2 nanoparticles exhibit a significant capacity for oxygen storage and outstanding electron transport characteristics, enabling more efficient and rapid Oxygen Reduction Reactions (ORR) [83]. Additionally, CeO_2 nanoparticles demonstrate exceptional chemical stability and significant resistance to poisoning and corrosion, making them crucial for applications requiring long-term performance.

The morphology of CeO_2 nanoparticles is examined using High Resolution-Transmission Electron Microscopy (HR-TEM), and the outcome images of the samples are presented in Figure 9(c-f). The images indicate that the samples exhibit uniformity and lack any amorphous phase. According to FE-SEM data, they consist of uniform spherical particles that range in size from 13 nm to 30 nm. The samples that have been prepared exhibit a high degree of crystallinity. The Debye rings observed in the selected area electron diffraction (SAED) pattern as Figure 9(f) are indicative of the distinctive ring arrangement associated with the cubic fluorite structure, thereby confirming the poly-crystalline characteristics of the synthesized samples. The arrangement of the diffraction rings, progressing from the innermost to the outermost, aligns with the interplanar distances of the {111}, {200}, {220}, {311}, {222}, {331}, and {422} lattice planes within the CeO_2 fluorite structure. Most of the observed agglomerations consist of small-sized nanoparticles with a spherical shape, as well as those that are irregularly shaped ones. The dimensions of the larger nanoparticles measure 20 ± 10 nm, although instances of even larger sizes were also noted, as illustrated in Figure 9(d). And the SAED pattern for CeO_2 exhibits a well-defined

orientation, with the (111) facet being the most prominent crystalline plane [84]. The morphological findings are contrasted with existing literature and are presented in Table 6. According to Table 6, the bio-synthesized cerium oxide nanoparticles demonstrate superior efficiency in removing chromium and COD compared to other types of nanoparticles.

3.8 Chemical oxygen demand and chromium reduction analysis by various methods in actual tannery wastewater

A total of 100 mL of actual tannery wastewater was combined with 600 mL of Millipore water to facilitate degradation studies. From that, the wastewater sample was taken as the required volume of 300 mL. The sample with a COD of 2350 ppm underwent a series of experiments focused on COD degradation. These experiments included combinations such as H_2O_2 + sample, H_2O_2 + sample + Methanol, H_2O_2 + sample + Fe^{2+}, H_2O_2 + sample + UV irradiation, H_2O_2 + sample + cerium oxide, and H_2O_2 + sample + UV irradiation + cerium oxide. The results of these studies are depicted in Figure 10. The findings suggest that the occurrence of chromium in actual tannery wastewater enhances the production of hydroxyl radicals during its degradation process with hydrogen peroxide. The addition of methanol as a quenching agent confirms the presence of hydroxyl radicals. Figure 10 demonstrates that the addition of methanol leads to a substantial reduction in the degradation percentage, dropping from 42.6 to a mere 1.5. On the other hand, incorporating Fe^{2+}, it improves the degradation percentage as 48.1% [32]. The addition of UV light irradiation sources improves the COD reduction to 57.5%. This reduction can be increased to 63.8% by adding a catalyst, and further to 77.2% when both the cerium oxide and ultraviolet irradiation are used in conjunction.

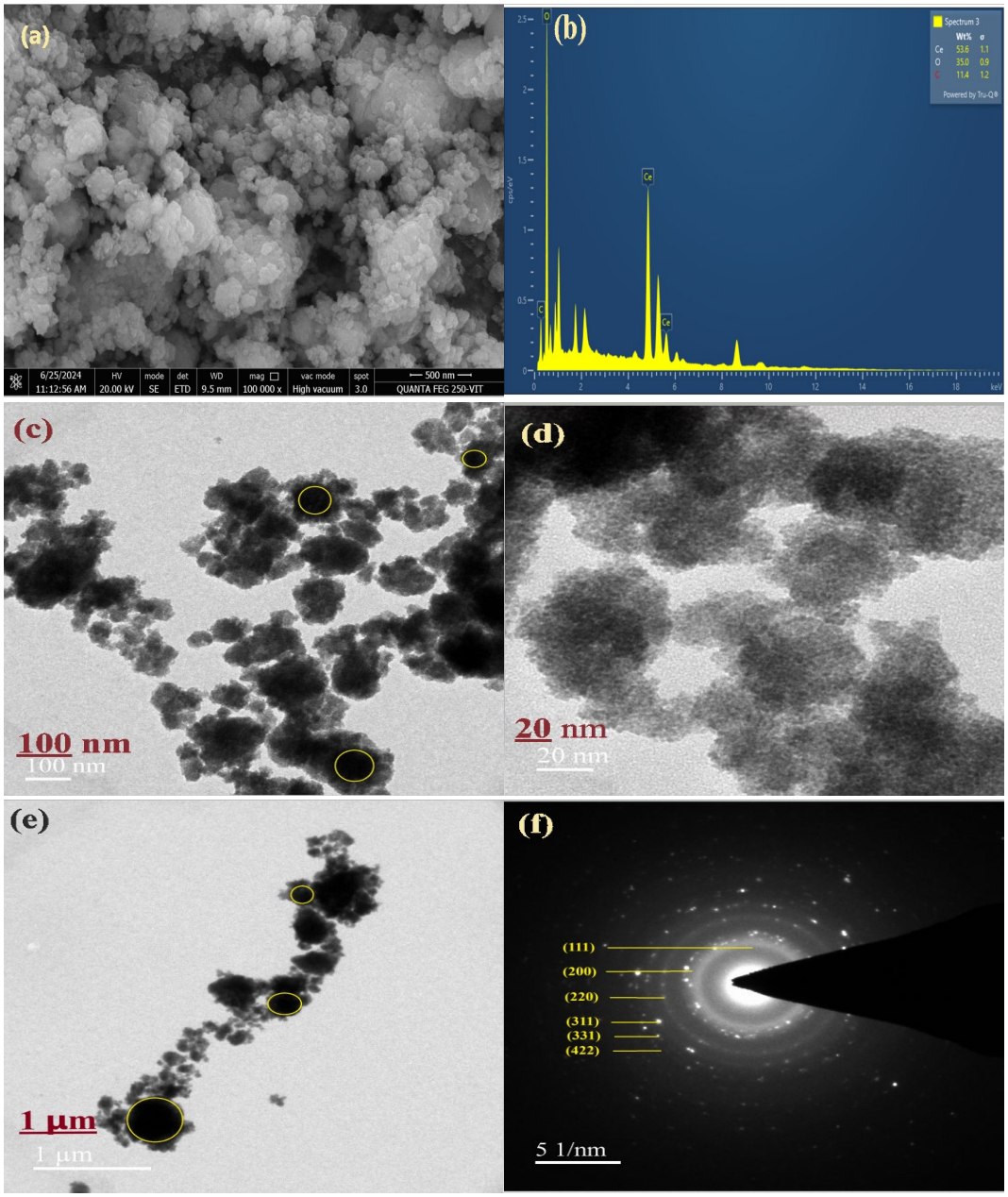

Figure 9. Nanoceria particles of (a) FE-SEM image, (b) EDAX spectra, (c-e) HR-TEM images, (f) SAED pattern.

Table 6. A literature survey of cerium oxide generated from various bio-synthesis.

Type of green extract used	pH ranges of the process	Nanoparticle size in ranges [nm]	Confirmation tests	Pollutant to be removed	Pollutant type	Efficiency [%]	Reference
Fresh leaves of *Azadirachta indica*	4 - 5	7.5 – 12	XRD, FTIR, SEM with EDX	Chromium and Cadmium	Synthetic	Cr = 93 Cd = 89	[85]
Jasminum officinale leaf extract	–	20 – 30	FTIR, XRD, SEM with EDX	Chromium removal in maize plants	Real	Cr = 70	[86]
Portulaca oleracea extract	7	4 – 17	FTIR, Raman, HRTEM	Methylene blue (MB) and Methylene Orange (MO)	Synthetic	MB = 98 MO = 95	[87]
Oroxylum indicum fruit extract	–	23.58	FTIR, UV-vis, SEM with EDX, XRD, and VSM	Methylene blue (MB)	Synthetic	56.77	[88]
Stevia rebaudiana extract	10	10 – 50	Raman, XRD, FTIR, FESEM	Tetracycline (TC)	Synthetic	80.68	[89]
Peepal leaves extract	11	13 – 30	UV-Vis., XRD, FTIR, BET, FESEM with EDX, and DLS	Cr(VI), COD	Real tannery wastewater	Cr(VI)=84.50 COD=77.02	This work

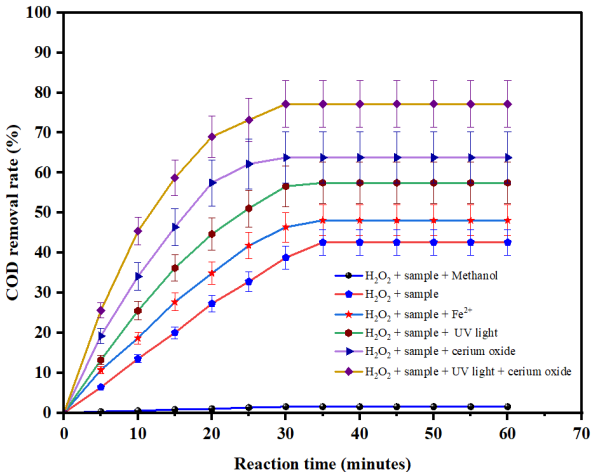

Figure 10. The photocatalytic effect of cerium oxide on tannery wastewater in various methods (Operating conditions: pH = 7, hydrogen peroxide = 0.0195 mL, cerium oxide = 0.04 g).

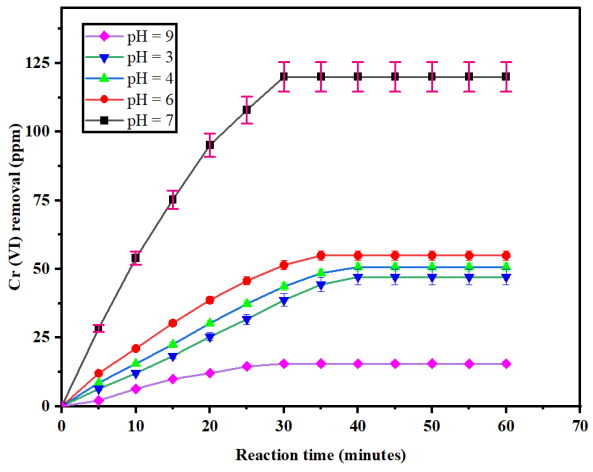

Figure 11. pH changes on chromium(VI) removal in tannery wastewater (Operating conditions: hydrogen peroxide = 0.0195 mL, cerium oxide=0.04 g).

Then, the concentration of Cr(VI) in the sample was assessed utilizing an atomic absorption spectrometer, which operates with an absorbance range exceeding 850 nm [85]. A chromium (VI) removal efficiency was 84.5% achieved in the wastewater sample with a combination of UV light irradiation, cerium oxide photocatalyst, and hydrogen peroxide dosage level. The integration of hydrogen peroxide, UV light irradiation, photocatalyst as cerium oxide dosage level on actual tannery waste-water resulted in a 77.2% decrease in chemical oxygen demand over a period of less than one hour, leading to further degradation investigations with this system. Additional verification using an alternative method was essential to confirm that the reduction in chromium absorbance resulted from the complete mineralization of the metal, rather than being solely associated with a redox reaction that lowered chemical oxygen demand.

3.9 Chromium removal by different pH conditions

Assessing the chromium level appears to be a fundamental initial step in evaluating the presence of chromium (VI). Diluting the sample is essential to ensure that the concentration of the analyte, which is chromium in this instance, falls within the linear range of the atomic absorption spectroscopy. Additionally, storing the sample in a sealed container is advisable to avoid contamination or the evaporation of volatile substances. Potassium dichromate is frequently selected for the preparation of chromium standards because of its excellent purity and stability. It is then diluted to create working standards at concentrations of 5 ppm, 10 ppm, and 15 ppm. More advanced atomic absorption spectroscopy is characterized by a double-beam with a detector of solid-state type, which typically enhances the performance regarding sensitivity, stability and the ability to analyze multiple elements simultaneously. A spectral bandpass of 0.12 nm is relatively narrow. Once the sample is injected, this narrow bandpass effectively isolates the specific wavelength associated with chromium absorption, minimizing the likelihood of interference from the absorption lines of other elements in the sample matrix or from molecular band absorption.

Graphite Furnace Atomic Absorption Spectroscopy (GFAAS), particularly when utilizing an advanced model such as the HGA 900 from PerkinElmer, provides exceptional sensitivity, enabling the identification of remarkably low levels of chromium. A study was carried out to assess the effectiveness of chromium removal by maintaining a pH of 7, employing a cerium oxide catalyst at a concentration of 0.04 g per 250 mL, and sustaining an H_2O_2 concentration of 0.0195 mL, all under room temperature conditions. The initial concentration of chromium was measured at 142 ppm. As illustrated in Figure 11, a chromium removal efficiency percentage of 84.5 was achieved within a frame of 60 min. An extra extension of time did not lead to any enhancements and resulted in a consistent state. Extended exposure durations of the cerium oxide nanoparticles catalyst affect the generation of radicals, resulting in a total reduction of ions, a decline in COD reduction, and a restriction of the oxidation effect. The dosage of the catalyst and extended operating durations are critical elements to consider when aiming to reduce Cr(VI), as these factors could lead to higher treatment expenses. This is attributed to the rapid oxidation of Cr^{3+} and the formation of $Cr(OH)_3$. In the process of photo-degradation, the combination of H_2O_2 and UV light rapidly generates hydroxyl (OH) radicals. As the duration of treatment extends, the generation of radicals decreases, resulting in a higher concentration of chromium(VI) derived from chromium(III) [86].

3.10 Chemical oxygen demand determination by pH effect

The pH of the solution plays a crucial role in all Fenton-like reactions. The generation of hydroxyl radicals, responsible for the oxidative degradation of various substrates, is significantly linked to the level of the solution pH. Research was carried out at pH levels of 3 and 9 to evaluate the effect of pH on the reduction of chemical oxygen demand in the chromium(VI) mediated Fenton-oxidation [87]. The results are depicted in Figure 12. The effectiveness of chemical oxygen demand removal increases as the pH level rises from 3 to 7. However, further increases in pH do not lead to any improvement in chemical oxygen demand removal efficiency. The most significant decrease in chemical oxygen demand was attained at a pH of 7. A pH level below 7 significantly hinders the reduction of COD. The various pH level of samples as shown in Figure 13.

Gradually the color changes from dark yellowish green to light green, then the color shifts to yellow, and finally colorless at pH 7. After 7 pH, the color is not reduced. This progression may be linked to the transformation of pollutants and warrants further investigation. This phenomenon arises from the increased concentrations of H^+, which act as a scavenger for $^{\bullet}HO$ radicals, as outlined in (Equation (22)) and additionally, as indicated in (Equation (23)), the H^+ ions from protonated hydrogen peroxide function as scavenger for $^{\bullet}HO$ radicals [88]. At pH levels below 7, $HCrO_4^-$ is the predominant species, whereas CrO_4^- becomes the primary species at pH levels above 7. $HCrO_4^-$ serves as a significantly stronger oxidizing agent compared to CrO_4^-, with a standard reduction potential of E0 ($HCrO_4^-/Cr^{3+}$ = 1.35 VSHE). This enhanced oxidizing capability allows $HCrO_4^-$ to facilitate oxidation at a faster rate than CrO_4^-, which has a standard reduction potential of E0 ($CrO_4^-/Cr(OH)_3$ = −0.13 VSHE) [89]. It can be concluded that a pH range of 6 to 7 is conducive to the reduction of chemical oxygen demand. Within 60 min, COD reduction of 77.02% was achieved under the optimum conditions, as of hydrogen peroxide dosage = 0.0195 mL, CeO_2 = 0.04 g/250 mL, at room temperature.

$$H_2O_2 + {}^{\bullet}OH \rightarrow {}^{\bullet}OOH + H_2O \quad (22)$$

$$^{\bullet}OOH + {}^{\bullet}OOH \rightarrow H_2O_2 + O_2 \quad (23)$$

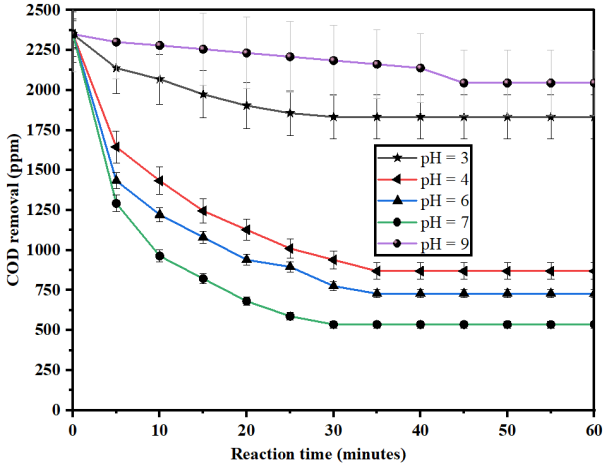

Figure 12. pH effect on chemical oxygen demand reduction in tannery wastewater (Operating conditions: hydrogen peroxide=0.0195 mL, cerium oxide=0.04 g).

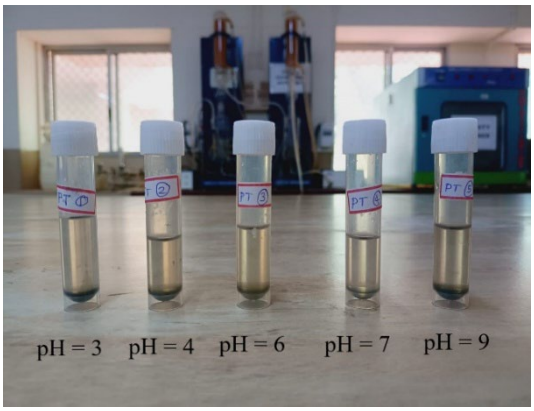

Figure 13. Hue changes in various pH adjustments on COD reduction.

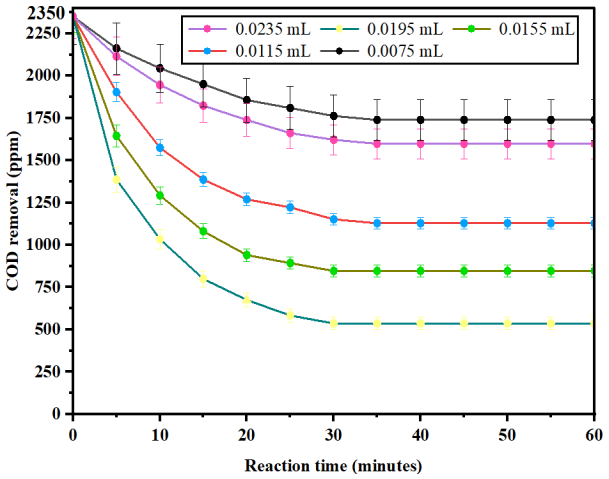

Figure 14. Hydrogen peroxide variations on COD in tannery wastewater (Operating conditions: pH=7, cerium oxide=0.04 g).

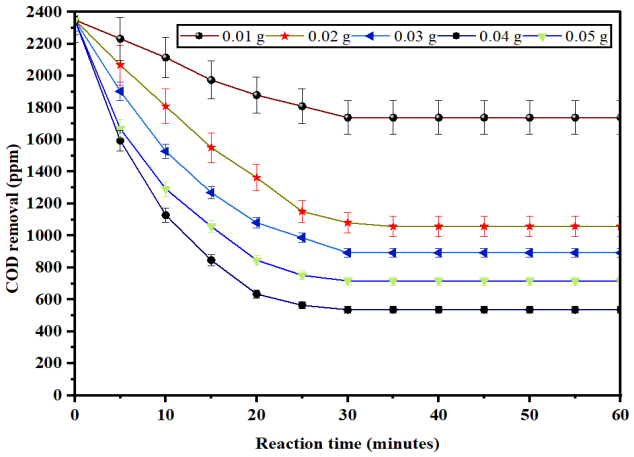

Figure 15. Cerium oxide photocatalyst effect on COD reduction in percentage on tannery wastewater (Operating conditions: pH=7, hydrogen peroxide=0.0195 mL).

3.11 COD determination by hydrogen peroxide effect

The impact of the varying H_2O_2 concentrations, ranging from 7.5 mM to 23.50 mM, on the reduction of COD in tannery wastewater was investigated, with the findings illustrated in Figure 14, and the data indicates that the efficiency of COD removal improved with an increase in H_2O_2 concentration. A maximum chemical oxygen demand removal rate of 77.02% was attained in under 45 min with a hydrogen peroxide (H_2O_2) dosage of 19.5 mM. This results from an increased generation of hydroxyl radicals within the system. An additional rise in H_2O_2 concentration did not enhance the degradation process; rather, it resulted in a reduction of COD removal efficiency. Similar results have been reported in the literature review, which can be linked to the self-scavenging effect of (H_2O_2) hydrogen peroxide in the system, as demonstrated in (Equation (24)). Although other radicals, including $^{\bullet}HO_2$ and O_2^{-}, are produced during the reaction, they exhibit lower reactivity and are therefore disregarded [90]. Consequently, a concentration of 0.0195 mL of hydrogen peroxide was selected for effective degradation.

$$H_2O_2 + {}^{\bullet}OH \rightarrow H_2O + {}^{\bullet}OH_2/{}^{\bullet}O_2^{-} \quad (24)$$

3.12 Effect of cerium oxide on COD reduction

The amount of catalyst used is a crucial factor affecting the effectiveness of targeted pollutants reduction [91]. Investigations were conducted to determine by the cerium oxide dosage on the removal of chemical oxygen demand and the removal of chromium (VI), with the findings illustrated in Figure 15. The information illustrated in the figure demonstrates that increasing the photocatalyst dosage from 0.01 g to 0.05 g per 250 mL, the reduction in chemical oxygen demand improved significantly, increasing from 26% to 77.02%. An additional increase in the dosage of the catalyst does not enhance the reduction of COD; rather, it results in a decrease in COD reduction. The highest level of photodegradation was achieved using 0.04 g of cerium oxide in a 250 mL of wastewater sample. The production of hydroxyl radicals increases with a higher dosage of the photocatalyst, as this enhances the catalyst's ability to absorb light. High concentrations of photocatalysts can lead to turbidity, which obstructs the light irradiation from penetrating the sample [92,93]. Additionally, excessive concentration of photocatalyst in the solution may lead to the aggregation of photocatalyst particles, thereby diminishing the pore of the catalyst [23].

Additionally, excessive cerium oxide concentration in the solution may lead to the aggregation of photocatalyst particles, thereby diminishing the surface area of the active sites within the catalyst [30]. The rate of COD removal from wastewater remained consistent as the concentration of penetration increased, indicating that the metal loading capacity of the catalyst had reached its saturation point.

Table 7 presents a comparison of different preparation methods for nanoceria particles along with their effectiveness as demonstrated by the current experimental findings. From Table 7, it was observed that it is highly comparable with the data available in the literature. Dainel *et al.,* reported that the CeO_2 photocatalyst attained 93% efficiency in the removal of Methylene Blue (MB) dye under visible light irradiation within a duration of 120 min [94]. In a similar manner, 90% degradation was attained under visible light exposure in wastewater containing indigo carmine dye, utilizing a cerium oxide catalyst produced by the sol-gel method [95]. Another sol-gel method produced cerium oxide achieved 50% MB dye degradation under the solar light radiation within 120 min [34]. This study anticipated that the PL extract generated a cerium oxide photocatalyst, which was assessed for the first time in actual tannery wastewater when exposed to UV light for 60 min, resulting in a reduction of Cr(VI) and COD by 84.5% and 77.2% respectively.

3.13 Kinetic study outcomes by various models

The experimental data fitted with various kinetic equations and the corresponding graphs are shown in Figure 16(a-d). The first order rate constant and R^2 values under different experimental conditions are given in the Table 8. The results indicated that the maximum constant value was achieved in run number 4. The comparison of other kinetic constants obtained with run 4 are shown in Table 9. The kinetic constants K1, K2, K3, and K4 were calculated from the figures based on the Least Square (LSQ) method as 0.0597, 0.0075, –2.0578 and –0.3999 respectively [96]. The second-order, diffusional, and Singh models have low and negative rate constant values indicates that, these kinetic models are not fitted with the degradation process and confirmed that they follow first order kinetics [97,98].

3.14 Repeatability experiment for recycling ability

The stability and reusability of a catalyst represent another crucial element in assessing its potential for practical application [99]. The sequence of catalyst recycling experiments was conducted to examine the photostability of the cerium oxide nanoparticles. The collection of catalyst from the aliquots sample was done by centrifugation, washed with Millipore water, and allowed to dry with 50°C, then are allowed to the next cycle of the experiment. All other experimental parameters remained unchanged from those established in the beginning trial. The UV irradiation period for each run is set at 60 min. The information illustrated in Figure 17 demonstrates that the COD degradation rate after the first cycle is 77.02%, whereas the removal rate noted after the final cycle is 75.0%. The decrease in Cr(VI) concentration from

wastewater, observed after the initial cycle, was 84.5%, while after the fourth cycle, it measured as 80.25%. The experimental results demonstrate that the catalytic performance of cerium oxide remains predominantly stable after 4 cycles, with no evidence of catalyst particle aggregation observed. The effectiveness of cerium oxide was observed to decline with an increasing number of runs, which is attributed to the accumulation of degraded molecules on its surface. This may be due to the slight morphological changes on the catalyst surface, which was observed in FTIR spectrum as shown in Figure 7(b).

Table 7. A comparative survey of the cerium oxide catalytic efficiency by various synthesis.

Photo-catalyst	Prepared methods	Light energy sources	Pollutants removed	Characteristic processes	Time progress	Parameters used level	Efficacy in percentages	References
CeO_2-NPs	One pot method	300 W Xe UV lamp	Tetracycline (synthetic wastewater)	XRD, PL, XPS, SEM, FTIR, EDS, UV-VIS, and DRS	1 h	Catalyst: 10 mg (10 ppm dye), pH = 7	76	[105]
Cerium oxide nanoparticles	Precipitation method	Fluorescent lamp (125 W)	Rhodamine-B (Rh-B) dye	SEM, XRD, FTIR and BET	5 h	Catalyst: 0.25g/50 mL of 10 ppm Rh-B	12	[106]
CeO_2 nanoparticles	Biosynthesis	400 W Xenon lamp	Textile wastewater	DSC analysis, HRTEM, XRF, XRD, FTIR, and Raman	270 min	Catalyst : 20 mg/100 mL of textile wastewater	80	[107]
CeO_2 nano photocatalyst	Biosynthesis	Visible light irradiation	Methylene blue dye	XRD, BET, FEG-SEM, particle size and UV spectroscopy	120 min	pH = 4, catalyst = 1 $g{\cdot}L^{-1}$, dye concentration = 60 $mg{\cdot}mL^{-1}$ at room temperature	93, and R^2 value from ANN = 0.999	[94]
Cerium oxide photocatalyst	Sol-gel method	Visible light source	Indigo carmine dye	SEM, XRD, XPS, FTIR and UV, and particle size distribution	180 min	pH = 5.6, dye concentration = 30 ppm, catalyst dosage = 60 mg/100 mL dye solution	90	[95]
CeO_2 nano photocatalyst	Sol-gel auto-combustion method	Solar light used	Methylene blue dye	UV-vis., XRD, HR-TEM, Raman and FTIR	120 min	Catalyst dosage = 20 mg, dye concentration = 10 ppm, pH = 7	50	[34]
Nanoceria photocatalyst particles	Bio-synthesis	36 W UV lamp	BOD & Chromium from actual tannery wastewater	UV-vis, FTIR, XRD, BET, FE-SEM, HR-TEM, zeta potential and Raman analysis	60 min	Catalyst = 40 mg/250 mL	Cr(VI)=84.5 COD=77.02	This work

Table 8. The kinetic study of Pseudo-first order model regression values.

Trail No.	Cerium oxide [g]	Hydrogen peroxide [mL]	pH level	Values of K_1 [min^{-1}]	Values of R^2
1	0.01	0.0195	7	0.0105	0.9974
2	0.02	0.0195	7	0.027	0.9983
3	0.03	0.0195	7	0.0358	0.9906
4	0.04	0.0195	7	0.0597	0.9906
5	0.05	0.0195	7	0.0458	0.9813
6	0.04	0.0195	3	0.0096	0.9724
7	0.04	0.0195	4	0.0349	0.9701
8	0.04	0.0195	6	0.043	0.958
9	0.04	0.0195	7	0.0597	0.9906
10	0.04	0.0195	9	0.0025	0.9919
11	0.04	0.0075	7	0.0108	0.9843
12	0.04	0.0115	7	0.0277	0.971
13	0.04	0.0155	7	0.0407	0.9642
14	0.04	0.0195	7	0.0597	0.9906
15	0.04	0.0235	7	0.0141	0.9818

Table 9. Pseudo-first, second, Diffusional, and Singh model kinetic values.

Types of kinetic rate order models	Values of Rate constants (K) [min^{-1}]	Values of R^2
Pseudo-first order rate values	K_1 = 0.0597	0.9906
Pseudo-second order rate values	K_2 = 0.0075	0.9583
Diffusional model	K_3= -2.0578	0.9478
Singh model	K_4= -0.3999	0.9903

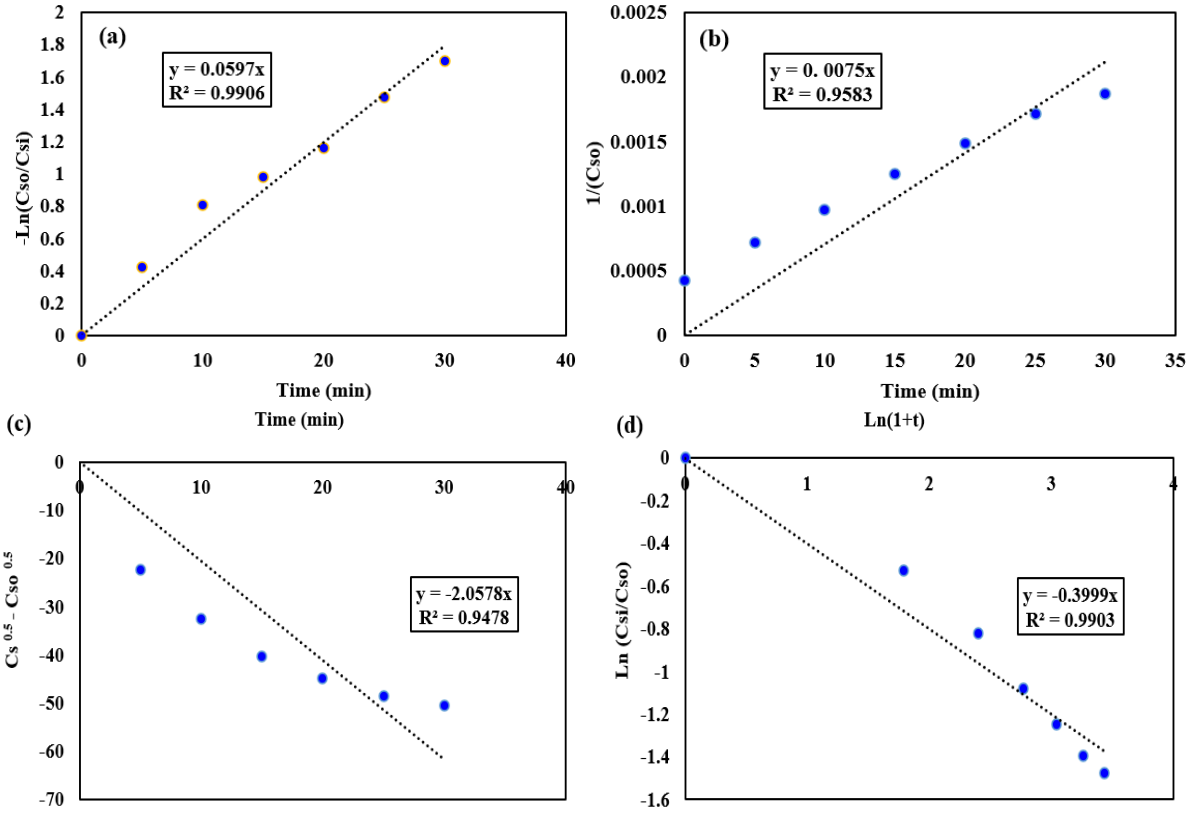

Figure 16 Tannery wastewater degradation kinetics (a) Pseudo – first order, (b) Pseudo – second order, (c) Diffusional model, and (d) Singh model.

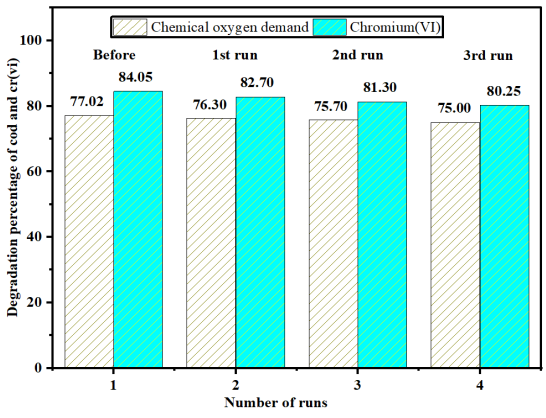

Figure 17. The stability of cerium oxide photocatalysts when subjected to UV irradiation.

4. Conclusion

This research focused on the production of cerium oxide particles via a bio-synthesis approach, employing Peepal Leaf extract alongside ammonium ceric nitrate and utilizing an ultrasonicated hydrothermal method. Ceria nanoparticles display a spherical shape, with the nano size ranging from 14.7 to 20.9, as assessed by field emission scanning electron microscopy and Debye-Scherrer's methods. Furthermore, the characterization of cerium oxide particles was conducted using UV-vis spectroscopy, X-ray diffraction, High-resolution transmission electron microscopy, Fourier-transform infrared spectroscopy, Brauner-Emmett-Teller analysis, and dynamic light scattering. The zeta potential value of – 28.65 mV indicates that the stability of the cerium oxide nanoparticles is good. This environmentally friendly synthesized nano-particle demonstrated effective performance in reducing chromium levels and chemical oxygen demand, establishing itself as a highly efficient photocatalyst. Additionally, this research sought to determine the optimal conditions for the photodegradation of tannery wastewater through a batch process. 77.02% of COD and 84.5% of Cr(VI) removal was achieved at an optimum condition of 16 mg·L^{-1} of catalyst dosage, 0.0195 mL of hydrogen peroxide, at a pH level of 7. Furthermore, under the optimum conditions, the degradation studies exhibit pseudo first-order kinetics, with the rate constant and R2 value of 0.0597 min^{-1} and 0.9906 respectively. These findings indicate that the cerium oxide nanoparticles synthesized through bio-synthesis method possess significant potential for degrading tannery wastewater.

Author contribution

All authors have contributed to the study, design, and conception. Writing drafts, methodology, and investigation, were performed by Ganeshkumar Govindasamy. Editing, reviewing, writing, and supervision, were performed by Arjunan Babu Ponnusami. All authors read and approved of the final manuscript.

Statements and declarations

Ethical approval: The authors declare that ethical approval is not applicable.

Consent to participate: Not applicable.

Consent for publication: Not applicable.

Competing interests: The authors declare that there are no competing interests.

Funding: The authors declare that no funds, grants, or other support were received during the preparation of this manuscript.

Availability of data and materials: Most data generated or analyzed during this study are included in this published article.

References

[1] R. Zhu, Q. Xu, X. Xiqiang, M. Sibt-e-Ali, M. Waqas, I. Ullah, A. Anwar, "Role of resources rent, research and development, and information and communication technologies on CO_2 emissions in BRICS economies," *Resources Policy*, vol. 93, p. 105072, 2024.

[2] S. Li, C. You, Q. Xue, Y. Zhao, F. Yang, Y. Liu, L. Bai, M. Zhang, and C. Zhuang, "Carbon quantum dots and interfacial chemical bond synergistically modulated S-scheme $Mn_{0.5}Cd_{0.5}S$/BiOBr photocatalyst for efficient water purification," *Journal of Materials Science & Technology,* vol. 214, pp. 255–265, 2025.

[3] Y. Liu, X. Xie, A. Tursun, Y. Wang, F. Jiang, and B. Zheng, "Surface water expansion due to increasing water demand on the Loess Plateau," *Journal of Hydrology: Regional Studies,* vol. 49, p. 101485, 2023.

[4] M. Al-Addous, M. Bdour, M. Alnaief, S. Rabaiah, and N. Schweimanns, "Water resources in jordan: A review of current challenges and future opportunities," *Water*, vol. 15, p. 3729, 2023.

[5] W. Musie, and G. Gonfa, "Fresh water resource, scarcity, water salinity challenges and possible remedies: A review," *Heliyon*, vol. 9, p. e18685, 2023.

[6] N. F. Shayan, N. Mohabbati-Kalejahi, S. Alavi, and M. A. Zahed, "Sustainable development goals (SDGs) as a framework for corporate social responsibility (CSR)," *Sustainability,* vol. 14, no. 3, p. 1222, 2022.

[7] *Sustainable development goal 6 : synthesis report 2018 on water and sanitation*. United Nations Publications, 2018.

[8] Y. C. Chang, and X. Zhao, "Addressing Japan's disposal of nuclear-contaminated water from the perspective of international human rights law," *Chinese Journal of Population, Resources and Environment*, vol. 22, no. 1, pp. 1–9, 2024.

[9] L. Lin, H. Yang, and X. Xu, "Effects of water pollution on human health and disease heterogeneity: A review," *Frontiers in Environmental Science*, vol. 10, p. 880246, 2022.

[10] S. Biswal, A. Subhadarshini, S. A. Behera, P. G. R. Achary, and B. Nanda, "Photodegradation of malachite green using 2D g-C_3N_5 nanosheet: A promising metal free catalyst," *Journal of Metals, Materials and Minerals*, vol. 35, no. 2, pp. 1–10, 2025.

[11] F. C. C, T. Kamalesh, P. S. Kumar, and G. Rangasamy, "A critical review on the sustainable approaches for the removal of toxic heavy metals from water systems," *Industrial & Engineering Chemistry Research*, vol. 62, no. 22, pp. 8575–8601, 2023.

[12] F. F. Qureshi, M. A. Ashraf, R. Rasheed, I. Hussain, M. Rizwan, M. Iqbal, and J. W. H. Yong, "Microbial-assisted alleviation of chromium toxicity in plants: A critical review," *Plant Stress*, vol. 11, p. 100394, 2024.

[13] H. Wang, "Advantages of animal leather over alternatives and its medical applications," *European Polymer Journal*, vol. 214, p. 113153, 2024.

[14] X. Chen, L. Xu, Z. Ren, F. Jia, and Y. Yu, "Sustainable supply chain management in the leather industry: A systematic literature review," *International Journal of Logistics Research and Applications*, vol. 26, no. 12, pp. 1663–1703, 2023.

[15] A. Moges, T. T. I. Nkambule, and J. Fito, "The application of GO-Fe_3O_4 nanocomposite for chromium adsorption from tannery industry wastewater," *Journal of Environmental Management,* vol. 305, p. 114369, 2022.

[16] G. El Mouhri, I. Elmansouri, H. Amakdouf, H. Belhassan, R. Kachkoul, F. E. El Oumari, M. Merzouki, and A. Lahrichi, "Evaluating the effectiveness of coagulation–flocculation treatment on a wastewater from the moroccan leather tanning industry : An ecological approach," *Heliyon*, vol. 10, no. 5, 2024.

[17] M. Nigam, P. Mishra, P. Kumar, S. Rajoriya, P. Pathak, S. Singh, S. Kumar, and L. Singh, "Comprehensive technological assessment for different treatment methods of leather tannery wastewater," *Environmental Science and Pollution Research*, vol. 30, no. 60, pp. 124686–124703, 2022.

[18] M. E. Mahmoud, M. A. Khalifa, A. A. Attia, M. W. Helmy, and M. A. B. Al-Sherady, "Effective adsorptive uptake of hexavalent chromium ions from aqueous systems utilizing a superior activated nanobentonite@cobalt ferrite@carboxymethyl cellulose nanocomposite," *Journal of Molecular Liquids,* vol. 407, p. 125172, 2024.

[19] A. Shoaib, S. Khurshid, and A. Javaid, "Cloncurry buffel grass mitigated Cr(III) and Cr(VI) toxicity in tomato plant," *Scientific Reports*, vol. 12, no. 1, p. 20952, 2022.

[20] F. Kookhaee, A. S. T. Bafroee, and L. Jabalameli, "Isolation and characterization of chromium (VI) tolerant bacteria from tannery effluents," *Journal of Environmental Health Science and Engineering*, vol. 20, no. 1, pp. 443–458, 2022.

[21] T. Wang, Y. Sun, L. Bai, C. Han, and X. Sun, "Ultrafast removal of Cr(VI) by chitosan coated biochar-supported nano zero-valent iron aerogel from aqueous solution: Application performance and reaction mechanism," *Separation and Purification Technology*, vol. 306, p. 122631, 2023.

[22] A. Singh, and I. Kostova, "Health effects of heavy metal contaminants Vis-à-Vis microbial response in their bioremediation," *Inorganica Chimica Acta*, vol. 568, p. 122068, 2024.

[23] X. Li, Y. Chen, Y. Tao, L. Shen, Z. Xu, Z. Bian, and H. Li, "Challenges of photocatalysis and their coping strategies," *Chem Catalysis*, vol. 2, pp. 1315 – 1345, 2022.

[24] S. Moles, M. P. Ormad, J. Gomez, J. Szpunar, E. Bolea, and R. Mosteo, "Pilot plant approach combining photocatalysis and adsorption for antibiotics removal from slaughterhouse and urban wastewater treatment plant effluents," *Environmental Technology & Innovation*, vol. 34, p. 103586, 2024.

[25] P. Kumari, and A. Kumar, "Advanced Oxidation Process: A remediation technique for organic and non-biodegradable pollutant," *Results in Surfaces and Interfaces*, vol. 11, p. 100122, 2023.

[26] J. Zhang, G. Yu, C. Yang, W. Zhao, Z. Duan, H. Liu, S. Li, "Reinforced ROS generation and anti-photo corrosion for boosted photooxidation disinfection by ief-enhanced type II charge carrier dynamics," *SusMat*, vol. 5, no. 2, p. e70002, 2025.

[27] N. O. Etafo, M. O. Bamidele, A. Bamisaye, and Y. A. Alli, "Revolutionizing photocatalysis: Unveiling efficient alternatives to titanium (IV) oxide and zinc oxide for comprehensive environmental remediation," *Journal of Water Process Engineering*, vol. 62, p. 105369, 2024.

[28] D. M. Tejashwini, H. V. Harini, H. P. Nagaswarupa, R. Naik, V. V. Deshmukh, and N. Basavaraju, "An in-depth exploration of eco-friendly synthesis methods for metal oxide nanoparticles and their role in photocatalysis for industrial dye degradation," *Chemical Physics Impact*, vol. 7, p. 100355, 2023.

[29] M. Pavel, C. Anastasescu, R. N. State, A. Vasile, F. Papa, and I. Balint, "Photocatalytic degradation of organic and inorganic pollutants to harmless end products: assessment of practical application potential for water and air cleaning," *Catalysts*, vol. 13, p. 380, 2023.

[30] M. A. Hassaan, M. A. El-Nemr, M. R. Elkatory, S. Ragab, V. C. Niculescu, and A. El Nemr, "Principles of photocatalysts and their different applications: A review," *Topics in Current Chemistry*, vol. 381, p. 31, 2023.

[31] N. Goodarzi, Z. Ashrafi-Peyman, E. Khani, and A. Z. Moshfegh, "Recent progress on semiconductor heterogeneous photocatalysts in clean energy production and environmental remediation," *catalysts*, vol. 13, p. 1102, 2023.

[32] M. A. Al-Nuaim, A. A. Alwasiti, and Z. Y. Shnain, "The photocatalytic process in the treatment of polluted water," *Chemical Papers*, vol. 77, pp. 677–701, 2023.

[33] G. Martemucci, C. Costagliola, M. Mariano, L. D'andrea, P. Napolitano, and A. G. D'Alessandro, "Free radical properties, source and targets, antioxidant consumption and health," *Oxygen*, vol. 2, no. 2, pp. 48–78, 2022.

[34] Fauzia, M. A. Khan, M. Chaman, and A. Azam, "Antibacterial and sunlight-driven photocatalytic activity of graphene oxide conjugated CeO_2 nanoparticles," *Scientific Reports,* vol. 14, no. 1, p. 6606, 2024.

[35] W. Zhu, and A. R. Kamali, "Mechanochemical synthesis of molybdenum disulfide quantum dots with enhanced dye adsorption and photocatalytic performance," *Journal of Water Process Engineering*, vol. 53, p. 103903, 2023.

[36] F. Abu Bakar, and N. S. I. Mohd Foad, "Synthesis of TiO_2 photocatalyst with tunable optical properties and exposed facet for textile wastewater treatment," *Results in Optics*, vol. 13, p. 100545, 2023.

[37] N. Alam, F. Rehman, M. Sohail, and A. Mumtaz, "Efficient charge separation and transportation using 1D iron-sulfide@ titania heterojunctions as photoanodes for improved interface stability and photoelectrochemical activity to produce hydrogen," *New Journal of Chemistry*, vol. 48, no. 9, pp. 3998–4008, 2024.

[38] S. Li, C. You, K. Rong, C. Zhuang, X. Chen, and B. Zhang, "Chemically bonded $Mn_{0.5}Cd_{0.5}S$/BiOBr S-scheme photocatalyst with rich oxygen vacancies for improved photocatalytic decontamination performance," *Advanced Powder Materials*, vol. 3, p. 100183, 2024.

[39] A. Aldrees, H. Khan, A. Alzahrani, and S. Dan'azumi, "Synthesis and characterization of tungsten trioxide (WO_3) as photocatalyst against wastewater pollutants," *Applied Water Science,* vol. 13, no. 7, p. 156, 2023.

[40] D. Singh, K. M. Batoo, S. Hussain, A. Kumar, Q. H. Aziz, F. S. Sheri, H. Tariq, and P. Singh, "Enhancement of the photocatalytic activity of rGO/NiO/Ag nanocomposite for degradation of methylene blue dye," *RSC Advances*, vol. 14, no. 4, pp. 2429–2438, 2024.

[41] J. Zhang, A. Bifulco, P. Amato, C. Imparato, and K. Qi, "Copper indium sulfide quantum dots in photocatalysis," *Journal of Colloid and Interface Science*, vol. 638, pp. 193–219, 2023.

[42] S. Selvaraj, D. S. Patrick, V. S. Manikandan, G. A. Vangari, M. K. Mohan, and M. Navaneethan, "Synergistic effects of La-doping on ZnO nanostructured photocatalysts for enhanced MB dye degradation," *Surfaces and Interfaces*, vol. 51, p. 104538, 2024.

[43] J. Zhang, G. Yu, C. Yang, and S. Li, "Recent progress on S-scheme heterojunction strategy enabling polymer carbon nitrides C_3N_4 and C_3N_5 enhanced photocatalysis in energy conversion and environmental remediation," *Current Opinion in Chemical Engineering*, vol. 45, p. 101040, 2024.

[44] M. Keerthana, T. P. Malini, P. Kamaraj, P. A. Vivekanand, R. Arulnangai, S. J. S. Kumar, S. Hari Kumar, N. Arumugam, A. I. Almansour, K. Perumal, "Efficient photocatalytic degradation of water pollutant Brufen using lutetium doped cerium oxide nanoparticles synthesized by chemical precipitation method," *Journal of the Taiwan Institute of Chemical Engineers,* vol. 166, p. 105118, 2023.

[45] W. Wang, H. Ren, S. Huang, J. Li, Y. Lv, and L. Du, "Synthesis and photocatalytic properties of Cerium(IV) oxide graphene oxide composites," *Materials Letters*, vol. 369, p. 136724, 2024.

[46] R.. Baird, A. D. Eaton, E. W. Rice, and Laura. Bridgewater, *Standard Methods for the Examination of Water and Wastewater*. American Public Health Association, 2017.

[47] N. Fifere, A. Airinei, F. Doroftei, T. S. Ardeleanu, M. Dobromir, D. Timpu, and E. L. Ursu, "Phyto mediated-Assisted preparation of cerium oxide nanoparticles using plant extracts and assessment of their structural and optical properties," *International Journal of Molecular Sciences*, vol. 24, no. 10, p. 8917, 2023.

[48] P. Parab, A. Pawanoji, and A. Pawar, "Peepal (*Ficus religiosa*) leaf extract mediated green synthesis of lanthanum and cerium oxide nanoparticles: Characterization and potential biological applications," *Indian Journal of Chemistry,* vol. 63, no. 1, pp. 15–20, 2024.

[49] J. Mei, X. Gao, J. Zou, and F. Pang, "Research on photocatalytic wastewater treatment reactors: design, optimization, and evaluation criteria," *Catalysts*, vol. 13, p. 974, 2023.

[50] N. Yadav, "Cerium oxide nanostructures: Properties, biomedical applications and surface coatings," *3 Biotech*, vol. 12, p. 121, 2022.

[51] A. Ashar, I. A. Bhatti, M. Mohsin, M. Yousaf, H. Aziz, A. Gul, T. Hussain, and Z. A. Bhutta, "Enhanced solar photocatalytic activity of thermally stable I:ZnO/glass beads for reduction of Cr(VI) in tannery effluent," *Frontiers in Chemistry*, vol. 10, p. 805913, 2022.

[52] S. Li, K. Dong, M. Cai, X. Li, and X. Chen, "A plasmonic S-scheme Au/MIL-101(Fe)/BiOBr photocatalyst for efficient synchronous decontamination of Cr(VI) and norfloxacin antibiotic," *eScience*, vol. 4, no. 2, 2024.

[53] S. Limbu, and L. R. Singh, "Exploring luminescent color tunability and efficient energy transfer mechanism of a single-phased hexagonal nanophosphor for white light emitting diodes (WLEDs) application," *Journal of Alloys and Compounds*, vol. 970, p. 172580, 2024.

[54] R. Ghosh, S. Gopalakrishnan, T. Renganathan, and S. Pushpavanam, "Adsorptive colorimetric determination of chromium(VI) ions at ultra trace levels using amine functionalized mesoporous silica," *Scientific Reports*, vol. 12, no. 1, p. 5673, 2022.

[55] S. Sharma, I. Qadir, A. K. Atri, S. Singh, U. Manhas, and D. Singh, "Solvent-free combustion-assisted synthesis of $LaFe_{0.5}Cr_{0.5}O_3$ nanostructures for excellent photocatalytic performance toward water decontamination: The effect of fuel on structural, magnetic, and photocatalytic properties," *ACS Omega*, vol. 8, no. 1, pp. 555–570, 2023.

[56] P. V. Gayathri, D. Nair, G. Gopinath, D. Pilla, and S. Joseph, "Solar photocatalysis for the decontamination of water from emerging pharmaceutical pollutant chloroquine using nano ZnO as the catalyst," *Water Air Soil Pollut*, vol. 234, no. 3, p. 146, 2023.

[57] X. Yu, S. Tong, M. Ge, L. Wu, J. Zou, C. Cao, and W. Song, "Adsorption of heavy metal ions from aqueous solution by carboxylated cellulose nanocrystals," *Journal of Environmental Sciences*, vol. 25, no. 5, pp. 933–943, 2013.

[58] S. Hokkanen, A. Bhatnagar, E. Repo, S. Lou, and M. Sillanpää, "Calcium hydroxyapatite micro fibrillated cellulose composite as a potential adsorbent for the removal of Cr(VI) from aqueous solution," *Chemical Engineering Journal*, vol. 283, pp. 445–452, 2016.

[59] L. Hao, P. Wang, and S. Valiyaveettil, "Successive extraction of As(V), Cu(II) and P(V) ions from water using spent coffee powder as renewable bio adsorbents," *Scientific Reports,* vol. 7, p. 42881, 2017.

[60] S. Ogunniyi, E. C. Emenike, K. O. Iwuozor, J. O. Ighalo, A. O. Ezzat, T. L. Adewoye, A. Egbemhenghe, H. K. Okoro, A. G. Adeniyi, "Removal of phenol from wastewater using Luffa cylindrica fibers in a packed bed column: Optimization, isotherm and kinetic studies," *Heliyon*, vol. 10, no. 4, p. e26443, 2024.

[61] A. Sharma, N. Kaur, A. Nanda, M. Kaur, R. Sharma, and H. S. Sohal, "Recent advances in synthesis and bio-applications of natural stabilizers for metal nanoparticles," *Journal of Metals, Materials and Minerals*, vol. 34, no. 4, pp. 1–23, 2024.

[62] H. Nosrati, M. Heydari, and M. Khodaei, "Cerium oxide nanoparticles: Synthesis methods and applications in wound healing," *Materials Today Bio*, vol. 23, p. 100823, 2023.

[63] S. Gea, S. A. Situmorang, N. Pasaribu, A. F. R. Piliang, B. Attaurrazaq, R. M. Sari, K. M. Pasaribu, and S. Goutianos, "Facile synthesis of ZnO–Ag nanocomposite supported by graphene oxide with stabilized band-gap and wider visible-light region for photocatalyst application," *Journal of Materials Research and Technology*, vol. 19, pp. 2730–2741, 2022.

[64] P. Priyadharshini and K. Pushpanathan, "Synthesis of Ce-doped $NiFe_2O_4$ nanoparticles and their structural, optical, and magnetic properties," *Chemical Physics Impact*, vol. 6, p. 100201, 2023.

[65] A. L. Chibac-Scutaru, V. Podasca, I. A. Dascalu, and V. Melinte, "Exploring the Influence of synthesis parameters on the optical properties for various CeO_2 NPs," *Nanomaterials*, vol. 12, no. 9, p. 1402, 2022.

[66] P. Tzevelekidis, M. Theodosiou, A. Papadopoulou, E. Sakellis, N. Boukos, A. K. Bikogiannakis, G. Kyriakou, E. K. Efthimiadou, and C. A. Mitsopoulou, "Visible-light-activated antibacterial and antipollutant properties of biocompatible Cu-doped and Ag-decorated TiO_2 nanoparticles," *Heliyon*, vol. 10, no. 17, p. e35634, 2024.

[67] M. G. Mamatha, M. A. Ansari, M. Y. Begum, D. P. B., A. A. Fatease, U. Hani, M. N. Alomary, S. Sultana, S. M. Punekar, N. M. B., T. R. Lakshmeesha, and T. Ravikiran, "Green synthesis of cerium oxide nanoparticles, characterization, and their neuro-protective effect on hydrogen peroxide-induced oxidative injury in human neuroblastoma (SH-SY5Y) cell line," *ACS Omega*, vol. 9, no. 2, pp. 2639–2649, 2024.

[68] M. E. Ioannou, G. K. Pouroutzidou, I. Chatzimentor, I. Tsamesidis, N. Florini, I. Tsiaoussis, E. Lymperaki, P. Komninou, and E. Kontonasaki, "Synthesis and characterization of cerium oxide nanoparticles: effect of cerium precursor to gelatin ratio," *Applied Sciences,* vol. 13, no. 4, p. 2676, 2023.

[69] D. Ma, Q. Xue, Y. Liu, F. Liang, W. Li, T. Liu, C. Zhuang, Z. Zhao, and S. Li, "Manipulating interfacial charge redistribution in $Mn_{0.5}Cd_{0.5}S$/N-rich C_3N_5 S-scheme heterojunction for high-performance photocatalytic removal of emerging contaminants," *Journal of Materials Science Technology*, vol. 243, pp. 265–274, 2026.

[70] A. El-Habib, B. Brioual, M. Bouachri, J. Zimou, A. Aouni, M. Diani, and M. Addou, "Synthesis and characterization of Nd-doped CeO_2 thin films grown by spray pyrolysis method: Structural, optical and electrochemical properties," *Surfaces and Interfaces*, vol. 45, p. 103859, 2024.

[71] F. Orudzhev, A. Muslimov, D. Selimov, R. R. Gulakhmedov, A. Lavrikov, V. Kanevsky, R. Gasimov, V. Krasnova, and D. Sobola, "Oxygen vacancies and surface wettability: key factors in activating and enhancing the solar photocatalytic activity of

ZnO tetrapods," *International Journal of Molecular Sciences*, vol. 24, no. 22, p. 16338, 2023.

[72] A. Arumugam, C. Karthikeyan, A. S. Haja Hameed, K. Gopinath, S. Gowri, and V. Karthika, "Synthesis of cerium oxide nanoparticles using Gloriosa superba L. leaf extract and their structural, optical and antibacterial properties," *Materials Science and Engineering C*, vol. 49, pp. 408–415, 2015.

[73] G. Jozanikohan and M. N. Abarghooei, "The fourier transform infrared spectroscopy (FTIR) analysis for the clay mineralogy studies in a clastic reservoir," *Journal of Petroleum Exploration and Production Technology*, vol. 12, no. 8, pp. 2093–2106, 2022.

[74] H. M. Panneerselvam, Z. M. Riyas, M. R. Prabhu, M. Sasikumar, and E. Jeyasingh, "In vitro cytotoxicity assessment of bio-synthesized nanoceria against MCF-7 breast cancer cell lines," *Applied Surface Science Advances*, vol. 21, p. 100603, 2024.

[75] K. Shahzad, J. Fernandez-Garcia, M. I. Khan, A. Shanableh, N. A. Khan, and A. ur Rehman, "Formulation of bismuth (Bi_2O_3) and cerium oxides (CeO_2) nanosheets for boosted visible light degradation of methyl orange and methylene blue dyes in water," *Catalysts*, vol. 12, no. 10, p. 1197, 2022.

[76] A. Kumar, D. Tyagi, S. Varma, H. Chand, V. Krishnan, K. Bhattacharyya, and A. K. Tyagi, "Thermal catalytic mineralization of ortho-dichlorobenzene at low temperature: an in-situ FT-IR and XPS mechanistic investigation," *Materials Advances*, vol. 5, no. 3, pp. 1301–1331, 2023.

[77] N. A. Hasan, N. N. Wazir, M. Y. Samsudin, M. M. S. M. Sanizam, N. M. Ahmad, N. A. B. Hisham, Y. Yasin, and N. R. N. Masdek, "Evaluation of photoactive contents and antibacterial activities of green synthesized cerium oxide nanoparticles using Melastoma sp. leaf extract as the capping agent," *Heliyon*, vol. 10, no. 14, p. e34558, 2024.

[78] J. Lupa, K. Morlo, R. Dobrowolski, P. Legutko, A. Sienkiewicz, and A. Kierys, "Highly porous cerium oxide prepared via a one-step hard template method as an extremely effective adsorbent for arsenic species removal from water," *Chemical Engineering Journal*, vol. 474, p. 145750, 2023.

[79] B. M. Kurji and A. S. Abbas, "Comparative study of textural properties for various silica by nitrogen adsorption-desorption technique," *Egyptian Journal of Chemistry*, vol. 65, no. 13, pp. 313–320, 2022.

[80] S. Parameswaran, R. Bakkiyaraj, P. Shanmugam, S. Boonyuen, and T. Venugopal, "Investigation of biological efficacy assessment of cobalt-doped cerium oxide nanocomposites against pathogenic bacteria, fungi, and lung cancer cells," *Materials Chemistry and Physics,* vol. 321, p. 129496, 2024.

[81] A. Jiménez-Vázquez, R. Jaimes-López, C. M. Morales-Bautista, S. Pérez-Rodríguez, Y. Gochi-Ponce, and L. A. Estudillo-Wong, "Catalytic applications of natural iron oxides and hydroxides: A review," *catalysts*, vol. 15, p. 236, 2025.

[82] N. Lopez-Arago, M. Munoz, Z. M. de Pedro, and J. A. Casas, "Natural magnetite as an effective and long-lasting catalyst for CWPO of azole pesticides in a continuous up-flow fixed-bed reactor," *Environmental Science and Pollution Research*, vol. 31, no. 20, pp. 29148–29161, 2024.

[83] M. Waseem Mumtaz, H. Mukhtar, W. Miran, A. H. Alessa, A. Waleed, Z. Sarwar, and H. Ashraf, "Impact of CeO_2 modified cathode and PANI modified anode on tannery wastewater fed microbial fuel cell performance," *Saudi Journal of Biological Sciences*, vol. 31, no. 8, p. 104024, 2024.

[84] S. N. Matussin, F. Khan, P. Chandika, M. H. Harunsani, N. Ahmad, Y. M. Kim, W. K. Jung, and M. M. Khan, "α-Glucosidase inhibitory activity and cytotoxicity of CeO_2 nanoparticles fabricated using a mixture of different cerium precursors," *ACS Omega*, vol. 9, no. 1, pp. 157–165, 2024.

[85] A. Bratovcic, H. Buksek, C. Helix-Nielsen, and I. Petrinic, "Concentrating hexavalent chromium electroplating wastewater for recovery and reuse by forward osmosis using underground brine as draw solution," *Chemical Engineering Journal*, vol. 431, p. 133918, 2022.

[86] K. Hao, Z. Zhang, B. Wang, J. Zhang, and G. Zhang, "Mechanism of Cr (VI) reduction by Pichia guilliermondii ZJH-1," *Iranian Journal of Biotechnology*, vol. 20, no. 1, p. e3001, 2022.

[87] R. Pattanaik, R. Kamal, D. Pradhan, and S. K. Dash, "Efficacy of $BiFeO_3$ and $Bi_4Ti_3O_{12}$ towards photocatalytic degradation of MG and MB dyes: A comparative study under solar irradiation," *Journal of Metals, Materials and Minerals*, vol. 35, no. 1, p. e2228, 2025.

[88] C. Carlsson, B. Fégeant, E. Svensson, L. Wiklund, and M. Jonsson, "On the selectivity of radical scavengers used to probe hydroxyl radical formation in heterogeneous systems," *The Journal of Physical Chemistry C*, vol. 126, no. 30, pp. 12435–12440, 2022.

[89] B. Lei, C. Wang, R. Zhang, Z. Xue, and F. Chen, "One-step removal of hexavalent chromium in wide pH range using thiourea dioxide: the role of reactive species," *RSC Advances*, vol. 13, no. 16, pp. 10693–10702, 2023.

[90] H. A. El-Gawad, M. Y. Ghaly, N. F. El Hussieny, M. Abdel Kreem, and Y. Reda, "Novel collector design and optimized photo-fenton model for sustainable industry textile wastewater treatment," *Scientific Reports*, vol. 14, no. 1, p. 8573, 2024.

[91] C. Wang, K. Rong, Y. Liu, F. Yang, and S. Li, "Carbon quantum dots-modified tetra (4-carboxyphenyl) porphyrin/BiOBr S-scheme heterojunction for efficient photocatalytic antibiotic degradation," *Science China Materials,* vol. 67, no. 2, pp. 562–572, 2024.

[92] H. Zhou, H. Wang, C. Yue, L. He, H. Li, H. Zhang, S. Yang, and T. Ma, "Photocatalytic degradation by TiO_2-conjugated/coordination polymer heterojunction: Preparation, mechanisms, and prospects," *Applied Catalysis B: Environmental*, vol. 344, p. 123605, 2024.

[93] K. Khoirunisa, N. D. Lestari, E. T. Wahyuni, And T. A. Natsir, "Enhanced photocatalytic reduction of Cr(VI) under visible light a magnetically separable TiO_2–Fe/Fe_3O_4 photocatalyst prepared from iron rusty waste," *Journal of Metals, Materials and Minerals*, vol. 35, no. 1, p. e2162, 2025.

[94] D. M. Druzian, L. R. Oviedo, S. N. Loureiro, R. D. Wouters, B. S. Vizzotto, E. de O. Pinto, N. J. S. de Vanconcellos, Y. P. M. Ruiz, A. Galembeck, G. Pavoski, D. C. R. Espinosa, C. dos Santos, and W. L. da Silva, "Cerium oxide nanoparticles: Biosynthesis,

characterization, antimicrobial, ecotoxicity and photocatalytic activity," *Journal of Photochemistry & Photobiology, A Chemistry*, vol. 442, p. 114773, 2023.

[95] Á. G. Aponte, M. A. L. RamÍrez, Y. C. Mora, J. F. Santa, MarÍn, and R. B. Sierra, "Cerium oxide nanoparticles for color removal of indigo carmine and methylene blue solutions," *AIMS Materials Science*, vol. 7, no. 4, pp. 468–485, 2020.

[96] G. Korkmaz, N. Aktay, B. Palas, G. Ersöz, and S. Atalay, "Photo fenton-like oxidation of real textile wastewater: Operating conditions, kinetic modelling and cost analysis," *Chemical Engineering and Processing - Process Intensification*, vol. 204, p. 109951, 2024.

[97] G. Asefa, D. Negussa, G. Lemessa, and T. Alemu, "The study of photocatalytic degradation kinetics and mechanism of malachite green dye on Ni-TiO_2 surface modified with polyaniline," *Journal of Nanomaterials*, vol. 2024, p. 9089, 2024.

[98] G. Govindasamy, and A. B. Ponnusami, "Development and evaluation of hydrogen peroxide mediated zinc oxide photocatalytic nanoparticles from *Peepal* (*Ficus Religiosa*) leaf extract for the treatment of actual tannery wastewater," *Environmental Science Water Research & Technology,* vol. 11, no. 2, pp. 508–523, 2025.

[99] J. Zhang, W. Liu, B. Liu, X. Duan, Z. Ao, and M. Zhu, "Is single-atom catalyzed peroxymonosulfate activation better? Coupling with metal oxide may be better," *Chinese Journal of Catalysis*, vol. 59, pp. 137–148, 2024.

[100] N. Masood, M. A. Irshad, R. Nawaz, T. Abbas, M. A. Abdel-Maksoud, W. H. AlQahtani, H. AbdElgawad, M. Rizwan, and A. H. A. Abeed, "Green synthesis, characterization and adsorption of chromium and cadmium from wastewater using cerium oxide nanoparticles; reaction kinetics study," *Journal of Molecular Structure*, vol. 1294, p. 136563, 2023.

[101] M. Latif, S. Ali, M. Ahmad Ansari, A. Fawad Zahoor, and M. Nafees, "Exploring the potential of green synthesized cerium oxide nanoparticles in mitigating chromium toxicity in maize," *Journal of King Saud University - Science*, vol. 36, no. 8, p. 103323, 2024.

[102] K. Hkiri, H. Elsayed Ahmed Mohamed, S. Ghotekar, and M. Maaza, "Green synthesis of cerium oxide nanoparticles using Portulaca oleracea Extract: Photocatalytic activities," *Inorganic Chemistry Communications*, vol. 162, p. 112243, 2024.

[103] J. Mim, Mst. S. Sultana, P. K. Dhar, Md. K. Hasan, and S. K. Dutta, "Green mediated synthesis of cerium oxide nanoparticles by using *Oroxylum indicum* for evaluation of catalytic and biomedical activity," *RSC Advances*, vol. 14, no. 35, pp. 25409–25424, 2024.

[104] M. Malakootian, S. N. Asadzadeh, M. Mehdipoor, D. Kalantar-Neyestanaki, and N. Firouzeh, "Stevia rebaudiana leaf extract mediated green synthesis of cerium oxide nanoparticles for antibacterial activity and photocatalytic degradation of tetracycline," *Desalination and Water Treatment*, vol. 317, p. 100126, 2024.

[105] X. He, W. Qin, and Y. Xie, "Degradation of tetracycline with photocatalysis by CeO_2-loaded soybean powder carbon," *Nanomaterials*, vol. 13, no. 6, p. 1076, 2023.

[106] N. Turkten, and Y. Karatas, "A novel study on the synthesis, characterization, and photocatalytic activity of CeO_2 nanoparticles," *Kahraman Maras Sutcu Imam University Journal of Engineering Sciences*, vol. 27, no. 1, p. 190–198, 2024.

[107] S. Ravichandran, P. Thangaraj, P. Sengodan, and J. Radhakrishnan, "Biomimetic facile synthesis of cerium oxide nanoparticles for enhanced degradation of textile wastewater and phytotoxicity evaluation," *Inorganic Chemistry Communications*, vol. 146, p. 110037, 2022.